

# Faraday Discussions

Accepted Manuscript



This is an Accepted Manuscript, which has been through the Royal Society of Chemistry peer review process and has been accepted for publication.

Accepted Manuscripts are published online shortly after acceptance, before technical editing, formatting and proof reading. Using this free service, authors can make their results available to the community, in citable form, before we publish the edited article. We will replace this Accepted Manuscript with the edited and formatted Advance Article as soon as it is available.

You can find more information about Accepted Manuscripts in the [Information for Authors](#).

Please note that technical editing may introduce minor changes to the text and/or graphics, which may alter content. The journal's standard [Terms & Conditions](#) and the [Ethical guidelines](#) still apply. In no event shall the Royal Society of Chemistry be held responsible for any errors or omissions in this Accepted Manuscript or any consequences arising from the use of any information it contains.

This article can be cited before page numbers have been issued, to do this please use: P. P. Hymas and J. Conboy, *Faraday Discuss.*, 2024, DOI: 10.1039/D4FD00206G.

## ARTICLE

# Phosphatidylserine affinity for and flip-flop dependence on $\text{Ca}^{2+}$ and $\text{Mg}^{2+}$ ions

Preston P. Hymas, John C. Conboy\*

Received 00th January 20xx,  
Accepted 00th January 20xx

DOI: 10.1039/x0xx00000x

$\text{Ca}^{2+}$  ions are believed to play a crucial role in regulating lipid membrane asymmetry by modulating the activity of flippases, floppases, and scramblases. Dysregulation of  $\text{Ca}^{2+}$  homeostasis, and subsequent loss of phosphatidylserine (PS) lipid asymmetry, is associated with physiological conditions such as blood clotting, neurodegeneration, and apoptosis. Yet, despite the prominence of  $\text{Ca}^{2+}$  within regards to PS flip-flop, the specific actions of  $\text{Ca}^{2+}$  are not fully understood and detailed mechanisms remain elusive. Much focus has been placed on enzymatic interactions, while the endogenous interactions of  $\text{Ca}^{2+}$  ions with PS and the direct role  $\text{Ca}^{2+}$  ions play on maintaining PS asymmetry have not been characterized in detail, a potentially crucial gap in understanding. In the current study the determination of the binding affinity of  $\text{Ca}^{2+}$  ions to planar supported lipid membranes containing PS were measured via sum-frequency vibrational spectroscopy (SFVS). Evaluation of binding affinity obtained from SFVS peak area analysis yielded an affinity of  $1.3 \times 10^5 \text{ M}^{-1}$ . The rate of PS flip-flop was also measured in the presence and absence of  $\text{Ca}^{2+}$  via SFVS, with a nearly five-fold decrease in the rate of translocation when  $\text{Ca}^{2+}$  ions are present. Controls which tested  $\text{Mg}^{2+}$  with PS or phosphatidylcholine (PC) with  $\text{Ca}^{2+}$  did not show similar slowing effects, highlighting the specificity of the PS- $\text{Ca}^{2+}$  interaction. For the binary lipid mixture tested, the disparity in the PS flip-flop rate would be sufficient to produce an 82% PS asymmetry if  $\text{Ca}^{2+}$  ions are localized to one side of the membrane. These studies have important implications for the non-enzymatic role  $\text{Ca}^{2+}$  ions may play in the maintenance of PS asymmetry.

## Introduction

Lipid asymmetry in living cells has long been recognized,<sup>1-5</sup> though the details of how phospholipid asymmetry is established, maintained, and destroyed is the subject of continued debate. What is known is that lipids are asymmetrically distributed between the cytosolic and extracellular leaflets of the plasma membrane based on both headgroup structure and alkyl chain saturation.<sup>7, 8</sup> Lipids facing the extracellular environment are predominantly phosphatidylcholine (PC) and sphingomyelin (SM) lipids; conversely, the aminophospholipids phosphatidylethanolamine (PE) and phosphatidylserine (PS) are found enriched on the cytoplasmic leaflet. Of these lipid species, PC, SM, and PE are net neutral zwitterions, while PS headgroups are net negative. Notably, while detectable levels of externalized PE are known to be present, PS sequestration to the inner leaflet is essentially absolute. An outer neutral leaflet with an underlying negative inner leaflet contributes to a physiologically vital membrane potential.<sup>9</sup> The charge

differential maintained by this arrangement has been shown to be important to intracellular fusion, budding, and ion diffusion processes which help maintain internal homeostasis.<sup>4, 10-16</sup> Meanwhile, loss of asymmetry and the subsequent externalization of PS is essential to blood coagulation and the inability to express PS is a key characteristic of the clotting disorder Scott's syndrome.<sup>10, 13, 16-19</sup> Externalization of PS to the extracellular leaflet also serves as a signal for phagocytes to engulf and clear apoptotic cells.<sup>20</sup>

The origin of the asymmetric lipid distribution found in cells has been ascribed to the action of ATP-dependent enzymes known as flippases and floppases that flip or flop lipids inward or outward, respectively.<sup>2, 4, 13, 21-25</sup> Several PS-active flippases have been identified, such as ATP11A, ATP11C, and aminophospholipid translocase (APLT).<sup>23, 25-29</sup> The ability of these enzymes to deliver PS lipids to the inner leaflet has been established through various means, including monitoring the uptake of fluorescent PS lipid analogues such as 7-nitro-2-1,3-benzoxadiazol-4-yl-PS (NBD-PS) with or without active flippases or floppases present.<sup>27-31</sup> Yet, while deactivation of these enzymes will slow the uptake and transfer of newly delivered PS, loss of flippase activity does not itself lead to loss of existing PS asymmetry. PS externalization in dead or dying cells has therefore been attributed to a third class of proteins, scramblases, which are believed to actively destroy PS asymmetry as part of apoptosis.<sup>2, 10, 13, 25, 28, 31-38</sup>

Department of Chemistry, University of Utah, 315 S. 1400 E. RM 2020, Salt Lake City, UT 84112,

\* Footnotes relating to the title and/or authors should appear here.

Supplementary Information available: [details of any supplementary information available should be included here]. See DOI: 10.1039/x0xx00000x



Activation of the scrambling process is routinely linked to  $\text{Ca}^{2+}$  ions. Elevation of cytosolic  $\text{Ca}^{2+}$  through either the incorporation of ionophores such as A23187, which increases inward flux, or deactivation of Ca-ATPase via agonists like thapsigargin, which decreases outward flux, reliably result in PS externalization.<sup>1, 17, 34, 36, 39-42</sup> Williamson et al. have, through a series of papers involving PS staining with FTIC-labeled Annexin V, quenching of NBD- or doxylpentanoyl-labeled lipids, and examination of phospholipase degradation products, established scrambling activity to affect a wide variety of lipid species.<sup>4, 29, 32, 36, 37, 43-45</sup> Williamson's group has found that not only will elevated cytosolic  $\text{Ca}^{2+}$  lead to mixing of the native PC, SM, PE, and PS lipids, but also NBD or doxylpentanoyl-labeled variants. Further, Ca-induced mixing of even non-natural lipid analogues such as fatty-acid carnitine esters and trimethylammonium-diphenylhexatriene has also been shown.<sup>30, 41</sup> These data establish the scrambling process to be quite indiscriminate toward lipid structure, yet the mechanism for how exactly  $\text{Ca}^{2+}$  enhanced scramblases lead to lipid translocation is not well understood.

Despite the demonstration of Ca-induced lipid mixing over a wide range of cell strains and lipid types, the identities of the specific enzymes responsible are currently unclear. Several potential scramblases have been identified, such as phospholipid scramblase (PLSCR) and ABCA1, yet studies on their activity is decidedly mixed. PLSCR<sup>-/-</sup> knockout in mice platelets did not inhibit PS exposure.<sup>46</sup> In addition, studies on lymphocytes, macrophages, and fibroblasts of Tangier disease patients who do not express ABCA1 found Ca-induced scrambling of PS to remain active.<sup>47, 48</sup>

The lack of a defined, well-established mechanism for how  $\text{Ca}^{2+}$  may lead to externalized PS is notable, a deficiency compounded by the fact that the direct effect  $\text{Ca}^{2+}$  ions have on the rates of protein-free PS flip-flop are unknown. There is a wide body of literature, beyond the discussion of scramblase activation, which suggests that PS-Ca pairing is quite important. When observing mixed monolayers and bilayers of PS and PC in the presence of  $\text{Ca}^{2+}$  ions, phase segregation of PS and PC was observed.<sup>49-51</sup> Janshoff et al. found the process can be reversed via removal of the  $\text{Ca}^{2+}$  with ethylene glycol tetraacetic acid (EGTA), a chelating agent with a strong affinity for  $\text{Ca}^{2+}$ . Similar results were found by Papahadjopoulos, who noted both  $\text{Ca}^{2+}$  and  $\text{Mg}^{2+}$  ions affect PS-containing membranes.<sup>50, 52, 53</sup> Interestingly, although PS was responsive to both ions, only  $\text{Ca}^{2+}$  lead to phase segregation, and while  $\text{Mg}^{2+}$  elevated the lipid melting point,  $\text{Ca}^{2+}$  completely abolished the transition within the tested temperature range. The ability for  $\text{Ca}^{2+}$  to induce membrane disruptions over  $\text{Mg}^{2+}$  have also been observed in lipid vesicles. PS-containing vesicles have enhanced fusion and aggregation in the presence of  $\text{Ca}^{2+}$ , behaviors which were either absent or reduced in the presence of  $\text{Mg}^{2+}$ .<sup>11, 15, 51-54</sup>

The divergence in  $\text{Ca}^{2+}$  and  $\text{Mg}^{2+}$  behavior toward PS is notable considering that, like PS, the concentrations of these species differ drastically over the cell membrane boundary. In the extracellular media,  $\text{Ca}^{2+}$  is in the range of 1-2 mM, yet exists in the 100-200 nM range within the cytoplasm.<sup>55, 56</sup> Conversely,  $\text{Mg}^{2+}$  ions within the cytoplasm are in the range of 0.6 – 1 mM.<sup>55</sup> While  $\text{Ca}^{2+}$  influx is commonly stated as the cause of scramblase activation, there is data to suggest the existing concentration gradient of  $\text{Ca}^{2+}$  is an equally important factor. Hampton et al. found complexation of internal  $\text{Ca}^{2+}$  using the chelating agent 1,2-Bis(2-aminophenoxy)ethane-N,N,N',N'-tetraacetic acid tetrakis(acetoxymethyl ester) (BAPTA-AM) did not inhibit PS exposure, whereas chelation of external  $\text{Ca}^{2+}$  with EGTA lead to a reduction of exposed PS by 50% to 65%.<sup>57</sup> Further, Bratton et al. found PS expression could be achieved via UV irradiation of human leukaemia (HL-60) cells, but that the degree of expression was directly related to the external concentration of  $\text{Ca}^{2+}$ .<sup>26</sup> To test if irradiation had caused the cells to become more permeable to  $\text{Ca}^{2+}$  resulting in  $\text{Ca}^{2+}$  influx, the authors used fluorescence from fura-2-acetoxymethyl ester-loaded cells and found intracellular  $\text{Ca}^{2+}$  had only risen by 100 nM in an external media containing 1 mM Ca. Their results indicate the presence of  $\text{Ca}^{2+}$  was required for externalization even though  $\text{Ca}^{2+}$  flux was minimal.

The results of Hampton and Bratton, combined with the previously detailed evidence of strong a Ca-PS interaction, suggest the presence of  $\text{Ca}^{2+}$  may directly influence the rate of PS flip-flop and, by extension, the maintenance of PS lipid asymmetry in cellular membranes irrespective of postulated scramblase activity. The interaction of solvated ions and membrane lipids have previously been shown to have a pronounced effect on rates of translocation. Cheng and Conboy found that exposure to  $\text{Yb}^{3+}$  ions slowed 1,2-dipalmitoyl-*sn*-glycero-3-phosphocholine (DPPC) flip-flop by an order of magnitude, demonstrating the potency of ion-lipid interactions to modulate lipid flip-flop dynamics.<sup>58</sup> It is hypothesized here that PS externalization can may, at least in part, be attributed to an equilibration of PS toward the  $\text{Ca}^{2+}$  exposed leaflet of the bilayer by way of unequal rates of native, nonenzymatic flip and flop. Such a hypothesis does not preclude enzymatic activity, but rather aims to assist in the interpretation of enzymatic data by clarifying what behaviors can be explained through direct Ca-PS and Mg-PS competitive effects in the extracellular and intercellular environments, respectively.

The importance of the nonenzymatic flip-flop of PS is less characterized than the enzymatic behaviors, as lipid mixing dynamics are often approached with the starting assumption that the non-enzymatic or "native" lipid flip-flop is too slow to be relevant. Leaflet mixing is therefore viewed largely through the lens of active transport, hence an overall focus on scramblase driven PS movement. While there are several studies which find native flip-flop to be quite slow, the literature contains a wide variance in the reported rates of translocation. Methods such as electron



paramagnetic resonance (EPR),<sup>3</sup> nuclear magnetic resonance (<sup>1</sup>H NMR),<sup>59</sup> small angle neutron scattering (SANS),<sup>60-62</sup> fluorescence,<sup>28, 45</sup> and sum-frequency vibrational spectroscopy (SFVS)<sup>63-68</sup> have been applied to the problem, yet there is little consensus on specific rates.

Divergent results are generally ascribed to two experimental factors. Firstly, determined rates of flip-flop can be highly dependent on the presence of chemical labels like the 2,2,6,6-tetramethylpiperidine 1-oxyl (TEMPO) label used by Kornberg and McConnell's EPR study.<sup>3, 65</sup> Analyzing the influence of the TEMPO label employed in Kornberg and McConnell's original work, Liu and Conboy showed that native DPPC lipids flip-flopped nearly 50-fold faster than the TEMPO-DPPC analogue. Liu and Conboy's study was performed using SFVS of planar supported lipid bilayers (PSLBs), a methodology advantaged by being capable of measuring the flip-flop rates of unlabeled lipids. The PSLBs methodology is, however, counter to Kornberg and McConnell who had utilized vesicle membranes. The membrane model, planar or vesicle, is another factor which can influence flip-flop measurements.

An example of a label-free method which has been employed for vesicle models is <sup>1</sup>H NMR analysis of asymmetric large unilamellar vesicles (aLUVs).<sup>59, 69-73</sup> aLUV analysis provides DPPC flip-flop rates several orders of magnitude slower than those measured in PSLBs, hypothesized by Marquardt et al. to be due to defect-enhanced translocation in PSLBs near sub-micron holes in surface coverage.<sup>70</sup> The effect of surface defects can be minimized through the incorporation of a highly hydrated polymer cushion between the bilayer and surface support, but cannot be removed entirely.<sup>74-78</sup> The influence of surface defects on PSLB flip-flop kinetics may not, therefore, be entirely discounted. However, inconsistencies in reported flip-flop rates are not entirely explainable purely by planar versus vesicle membrane dynamics. The TEMPO-PC flip-flop observed by Kornberg and McConnell in DPPC is several orders of magnitude faster than DPPC flip-flop rates observed in aLUVs,<sup>3, 70</sup> despite the presence of the bulky TEMPO label. As both studies utilized vesicle models, the discrepancy would not be explainable by surface coverage defects.

While it is clear that methodological differences can influence the flip-flop rates obtained, the study herein is interested primarily in relative kinetic shifts which may affect the equilibrium of PS expression. In order to validate the Ca-modulated PS flip-flop hypothesis, the present study used SFVS of PS-containing PSLBs in the presence of physiologic 1 mM concentrations of Ca<sup>2+</sup> or Mg<sup>2+</sup> ions to compare their effects on PS flip-flop dynamics. Solutions were ionic strength matched and use a baseline comparison to 100 mM KCl to mimic the cytosolic environment where K<sup>+</sup> ions predominate.<sup>79</sup> As the utilized methodology was consistent among all samples examined, the Ca<sup>2+</sup> or Mg<sup>2+</sup> induced changes in lipid flip-flop kinetics are used to make inferences on *in vivo* PS lipid behaviour.

Gel phase mixtures of DPPC and 1,2-dipalmitoyl-*sn*-glycero-3-phosphoserine (DPPS) were utilized due to the inability to measure the rapid flip-flop mixing of liquid crystalline (LC) phase lipids by SFVS using PSLB model membranes. While binary mixtures of DPPC and DPPS are not physiologic, the simplified mixture allowed the variable of PS-selective Ca<sup>2+</sup> or Mg<sup>2+</sup> interactions to be isolated. Aside from headgroup identity these two lipids are structurally identical. Thus, any divergence in response to Ca<sup>2+</sup> or Mg<sup>2+</sup> exposure is attributed to differences in the binding of these two ions to PC and PS headgroups. Additionally, compression isotherms of lipid monolayers on subphases with or without Ca<sup>2+</sup> and Mg<sup>2+</sup> were used to probe the effects these ions have on the packing and compressibility of DPPS and DPPC lipids. Finally, SFVS of hybrid bilayers, composed of lipid monolayers deposited to a methylated silica surface, was utilized to determine the affinity of DPPS for Ca<sup>2+</sup> and Mg<sup>2+</sup> and characterize structural changes occurring within the headgroups, water solvation layer, and lipid alkyl chains.

### Sum-frequency Vibrational Spectroscopy

Sum-frequency vibrational spectroscopy is a coherent nonlinear optical method which involves simultaneous infrared (IR) excitation and anti-stokes Raman scattering to generate an outgoing photon at the sum of the two input energies.<sup>80</sup> In the present case, the system employed uses a tunable IR ( $\omega_{IR}$ ) and a fixed 532 nm visible ( $\omega_{532}$ ) laser to generate the sum-frequency beam ( $\omega_{S.F.}$ ):

$$\omega_{S.F.} = \omega_{532} + \omega_{IR} \quad (1)$$

Generation of the sum-frequency is dependent on the second order nonlinear susceptibility of the material ( $\chi^{(2)}$ ) and scaled by the linear transmission Fresnel coefficients of the IR ( $f_{IR}$ ) and 532 nm ( $f_{532}$ ), as well as the nonlinear Fresnel coefficient of the outgoing sum-frequency ( $\tilde{f}_{S.F.}$ ):

$$I_{S.F.} = |\tilde{f}_{S.F.} f_{532} f_{IR} \chi^{(2)}|^2 \quad (2)$$

The second order susceptibility is a third order, 27 element tensor which describes the coupling of the three electric field vectors (IR, visible, and sum-frequency) in three-dimensional space (x, y, and z).  $\chi^{(2)}$  contains both resonant ( $\chi_R^{(2)}$ ) and non-resonant ( $\chi_{N.R.}^{(2)}$ ) contributions, however the non-resonant component is small compared to the resonant component when dealing with dielectric materials and may usually be ignored:

$$\chi^{(2)} = \chi_R^{(2)} + \chi_{N.R.}^{(2)} \approx \chi_R^{(2)} \quad (3)$$

The resonant component ( $\chi_R^{(2)}$ ) is proportional to the number of molecules (N) at the interface, scaled by the IR ( $A_i$ ) and Raman ( $M_{jk}$ ) transition probabilities (Equation 4). Resonance will reach a maximum when the tunable IR ( $\omega_{IR}$ )



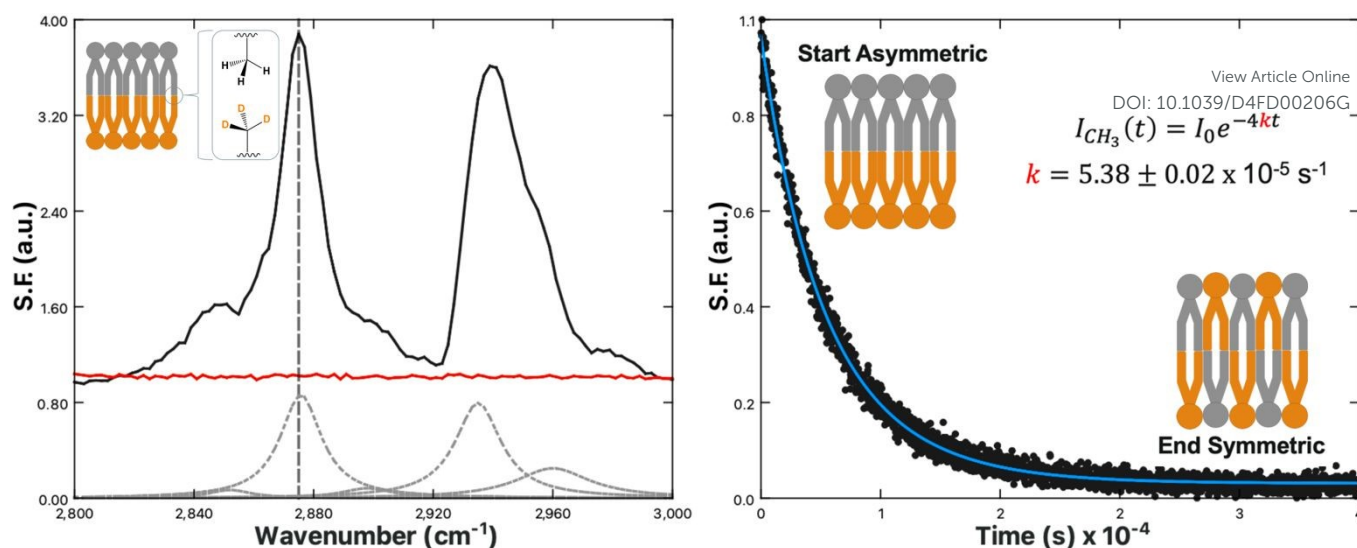


Figure 1: A) SFVS spectrum scan of an asymmetric DPPC/DPPC-d62 bilayer (black) and symmetric DPPC/DPPC bilayer (red). Inset image shows an illustration of an isotopically asymmetric lipid bilayer highlighting the terminal CH<sub>3</sub> symmetric stretch. The CH<sub>3</sub> symmetric stretch is located at 2875 cm<sup>-1</sup>, denoted with a vertical grey dashed line. The grey dashed curves are the fits to the various C-H resonances obtained by fitting the SFVS spectrum to Equation 4, with the data offset for clarity. B) SFVS intensity decay of the CH<sub>3</sub> symmetric stretch at 2875 cm<sup>-1</sup> for an asymmetric DPPC/DPPCd62 bilayer recorded at 28 °C. The solid blue line is the fit of the decay data using Equation 7.

) is matched to a vibrational mode ( $\omega_v$ ), though will be limited by the linewidth of the transition ( $\Gamma_v$ ). Expressed as a sum over all possible vibrational modes, the sum-frequency dependence on the total resonant contribution can be expressed as follows:

$$I_{SF} \propto |\chi_R^{(2)}|^2 = \left| \sum_v \frac{N \langle A_i M_{jk} \rangle}{\omega_v - \omega_{IR} - i\Gamma_v} \right|^2 \quad (4)$$

The orientation of the molecules is implicit via the bra ( $\langle$ ) and ket ( $\rangle$ ) operators, which denote an average of all molecular orientations. In isotropic media where the orientational averaging results in no net directionality, the expected sum-frequency is zero. Only in anisotropic media, or at an interface, should sum-frequency be observed.<sup>81</sup> Due to the symmetry dependence of the sum-frequency, SFVS can be utilized to great advantage when observing interleaflet mixing. Bilayer systems contain a natural plane of inversion between the leaflets, and thus any sum-frequency generated is proportional to the number difference of species in the proximal ( $N_{proximal}$ ) and distal ( $N_{distal}$ ) leaflets:<sup>64, 82</sup>

$$I_{SF} \propto (N_{proximal} - N_{distal})^2 \quad (5)$$

One technique to achieve lipid leaflet asymmetry is through the use of PSLBs prepared via the Langmuir-Blodgett/Langmuir-Schaeffer (LB/LS) transfer methods. Selective deuteration of the lipid tails in one leaflet shifts the resonances out of the C-H region into the C-D region, removing any interference of sum-frequency from the antiparallel orientation of the tails. This bilayer asymmetry allows the alkyl chain C-H vibrations to become sum-frequency active. Figure 1A illustrates this principal for the C-H vibrational region recorded for an asymmetric DPPC /

DPPCd62 bilayer and a symmetric DPPC/DPPC bilayer. Five key vibrational modes are observed: the CH<sub>2</sub> symmetric stretch at 2850 cm<sup>-1</sup>, CH<sub>3</sub> symmetric stretch at 2875 cm<sup>-1</sup>, CH<sub>2</sub> fermi resonance at 2905 cm<sup>-1</sup>, CH<sub>3</sub> fermi resonance at 2935 cm<sup>-1</sup>, and CH<sub>3</sub> asymmetric stretch at 2960 cm<sup>-1</sup>.<sup>65, 66</sup> The spectra in Figure 1 were collected with s-polarized sum-frequency, s-polarized 532 nm and p-polarized IR. This optical configuration probes the component of the vibrational transitions parallel to the surface normal. For this reason, the terminal CH<sub>3</sub> stretch appears most prominently in *ssp* spectra.

As the sum-frequency is proportional to the lipid number difference between the leaflets, changes in the sum-frequency (SF) intensity can therefore be attributed directly to mixing between the two leaflets:

$$N_{distal} \xrightleftharpoons[k_{flip}]{k_{flip}} N_{proximal} \quad (6)$$

where  $k_{flip}$  and  $k_{flop}$  are the rates of lipid translocation. By measuring the decay in intensity emanating from the CH<sub>3</sub> symmetric stretch ( $\nu_s$ ) at 2875 cm<sup>-1</sup>, lipid translocation can be observed without the use of fluorescent or spin-labelled lipids. A plot of the CH<sub>3</sub>  $\nu_s$  sum-frequency decay (Figure 1B) with time can be fit to Equation 7, derived by Liu and Conboy, which allows the rate constant of lipid flip-flop to be determined:<sup>66</sup>

$$I_{CH_3,t} = I_0 e^{-kt} \quad (7)$$

where  $I_{CH_3,t}$  is the sum-frequency at any time,  $t$ ;  $I_0$  is the starting intensity; and  $k$  is the rate of lipid flip-flop. Importantly, Equation 7 is derived under the assumption of equivalent environments within each leaflet such that  $k_{flip} = k_{flop}$ .



## Experimental

### Materials

All materials were used as received without further purification. 1,2-dipalmitoyl-*sn*-glycero-3-phosphocholine (DPPC), 1,2-dipalmitoyl-d62-*sn*-glycero-3-phosphocholine (DPPC-d62), 1,2-dipalmitoyl-*sn*-glycero-3-phosphoserine (DPPS), and 1,2-dipalmitoyl-d62-*sn*-glycero-3-phosphoserine (DPPS-d62) (Figure 2) were purchased from Avanti Polar Lipids (Alabaster, AL). 99.995% pure KCl (metals basis), ultra dry, 99.9% pure MgCl<sub>2</sub> (metals basis), Tris Base, HPLC-grade chloroform, and deuterium oxide were purchased from Thermo Fisher Scientific (Waltham, MA). Nanopure, 18.2 MΩ·cm water from a Barnstead Thermolyne (Dubuque, IA) system was used for all aqueous solutions.

Lipid stock solutions of DPPC, DPPC-d62, DPPS, and DPPS-d62 were made at 1 mg/mL in HPLC-grade chloroform. Mixtures of various PS:PC mol fractions were made using these parent solutions.

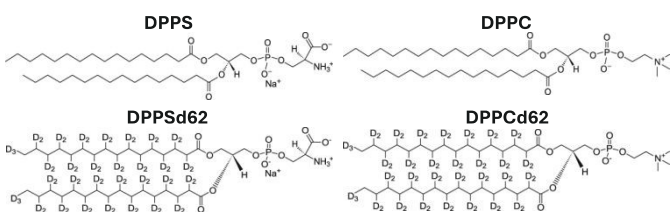


Figure 2: Chemical structures of protonated and deuterated DPPC and DPPC lipids.

### Compression Isotherms

Pressure-area isotherms were collected on a Langmuir trough (KSV, Helsinki, Finland). Prior to lipid additions, each subphase was checked for surface contaminants with a barrier sweep over the surface, with barrier compressions resulting in less than a 0.2 mN/m lateral surface pressure increase considered sufficient for lipid deposition. Lipid solutions in chloroform were deposited dropwise at the air-water interface and allowed to evaporate for 10 minutes. All monolayers were compressed at a rate of 4 mm/min at room temperature (21 °C).

### Silica Supports

Custom IR-grade fused silica prisms were purchased from Almaz Optics (Marlton, NJ). Before each use, prisms were cleaned for at least 10 minutes under ozone (Jetlight Co., Irvine, CA), followed by submersion in a 3:1 mixture of concentrated sulfuric acid and 30% H<sub>2</sub>O<sub>2</sub> for at least one hour. **Caution: Piranha solutions contain strong oxidants which react violently, potentially explosively, with organics. Submerged prisms should be absolutely free of any residual organic solvents, and extreme care with proper personal protective equipment should be used when handling these corrosive mixtures.** Finally, each prism was rinsed with

18.2 MΩ·cm water, dried under N<sub>2</sub>, and treated with argon plasma (Harrick Scientific, Ithaca, NY) for at least 10 minutes.

View Article Online

DOI: 10.1039/D4FD00206G

### Planar Supported Lipid Bilayers

PSLBs were deposited to silica prisms at a surface pressure of 30 mN/m to mimic physiological conditions.<sup>83</sup> Compressions were performed following the same procedure listed in the 'Compression Isotherms' section. To prevent interactions between the lipid headgroups and the silica surface, particularly salt bridging with PS, a 3% C16-PEG(5000)PE lipid fraction was incorporated for LB depositions (proximal leaflet). The highly water-soluble PEG groups attached to the lipid heads form a PEG polymer cushion to act as a spacer between the support and lipids.<sup>75-77, 84</sup> For LB depositions the prism was pulled up through the interface at a rate of 4 mm/min. For the LS deposition the prism was rotated 90° and aligned to be as perfectly level with the trough as possible. The trough was reset with a fresh subphase, new lipids of the desired composition, and compressed to 30 mN/m as previous. The prism was then brought back through the interface to deposit the distal leaflet.

### Hybrid Bilayers

Silica prisms were surface modified by submersion in a solution of 2% trimethoxymethylsilane in dry toluene (v/v) with an incubation time of at least one hour. Incubation should be performed in a covered container to prevent evaporation of the toluene. Following incubation, the surface was rinsed with methanol and placed into an oven at >80 °C for at least one hour. Finally, a lipid monolayer was deposited via a single LS transfer at 30 mN/m on the methylated surface to create a hybrid bilayer.

## Results and Discussion

### Compression Isotherms

The effect of Ca<sup>2+</sup> and Mg<sup>2+</sup> ions on lipid packing and compression were examined by way of pressure-area isotherms for three lipid systems: control monolayers of 100% DPPC (Figure 3A), monolayers of 10% DPPS in DPPC as a physiologically appropriate PS fraction (Figure 3B), and monolayers of 100% DPPS (Figure 3C). The subphases for all experiments were ionic strength matched, with a base solution of 100 mM KCl and 50 mM Tris buffer for a total ionic strength of 133.4 mM at pH 7.4. The amount of KCl present was reduced to 97 mM to compensate for the addition of 1 mM CaCl<sub>2</sub> or MgCl<sub>2</sub> when those species were present. Each experiment was performed at least three times and averaged.

In the absence of either Ca<sup>2+</sup> or Mg<sup>2+</sup>, the mean molecular areas (MMAs) at a physiological surface pressure of 30 mN/m were determined to be 49.3 ± 0.5, 45.9 ± 0.7, and 46.7 ± 0.7 Å<sup>2</sup>/molecule for the 100% PS, 100% PC, and 10% PS systems, respectively. The values



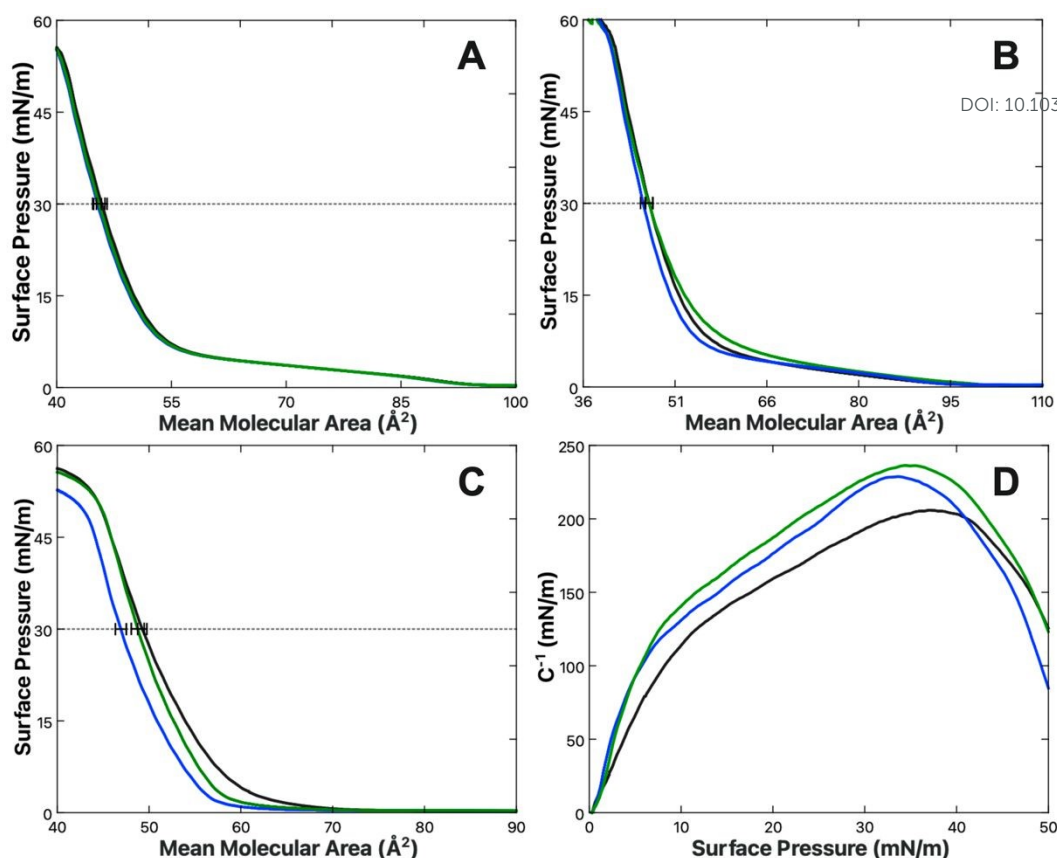
View Article Online  
DOI: 10.1039/D4FD00206G

Figure 3: Pressure-area isotherms of A) DPPC, B) 10% DPPS in DPPC, and C) DPPS obtained with a subphases of 100 mM KCl (black), 97 mM KCl + 1 mM CaCl<sub>2</sub> (blue) or 1 mM MgCl<sub>2</sub> (green). Each line represents the average of at least three replicate measurements. All subphases are buffered with 50 mM Tris at pH 7.4. D) Compression moduli of DPPS as a function of surface pressure, calculated from the isotherms displayed in (C) using Equation 7 for 100 mM KCl (black), 97 mM KCl + 1 mM CaCl<sub>2</sub> (blue) or 1 mM MgCl<sub>2</sub> (green). Compression moduli were obtained by employing a 50-point rolling average on the corresponding  $\pi$ -A isotherm.

determined for pure PC and PS agree favorably with those reported elsewhere.<sup>85, 86</sup> Upon the addition of 1 mM Ca<sup>2+</sup> or Mg<sup>2+</sup>, no net change in the MMA of DPPC was observed. A previous report from Allen et al. found DPPC monolayers to expand in the presence of Ca<sup>2+</sup>,<sup>87</sup> however, those studies were carried out at much higher concentrations of Ca<sup>2+</sup>, starting at 300 mM CaCl<sub>2</sub> compared to 1 mM here. Additionally, their baseline of comparison was a pure water subphase rather than ionic strength matched buffer. The divergent results can therefore likely be attributed to experimental differences between their study and the results found here.

More notable results are found in the DPPS mixtures where, when in the presence of Ca<sup>2+</sup>, but not Mg<sup>2+</sup>, there is a reduction in MMA of  $-0.2 \pm 0.7$  and  $-2.4 \pm 0.6$  Å<sup>2</sup>/molecule for 10% and 100% DPPS, respectively, at 30 mN/m surface pressure. In the case of the 10% DPPS system the differential is within the margin of error; however, the 100% DPPS system is significant and suggests a net condensation of the DPPS monolayer in the presence of Ca<sup>2+</sup> ions. Given the low mol fraction in the 10% mixture, one might expect only one-tenth the response as in the neat DPPS monolayer, corresponding to a shift of around  $-0.2$  Å<sup>2</sup>/molecule, which is within the standard deviation of the experiment. The 10% DPPS data therefore agrees within error. The condensing behavior

observed for Ca<sup>2+</sup> with pure PS monolayers is additionally consistent with behavior observed by Narayanan who found a contraction of 1,2-dilauroyl-sn-glycero-3-phospho-L-serine (DLPS) in the presence of 10 mM Ca<sup>2+</sup>.<sup>88</sup> Narayanan observed Mg<sup>2+</sup> to have a weaker condensing effect than Ca<sup>2+</sup>, with the condensation disappearing at higher surface pressures. A similar trend was observed here, with the Mg<sup>2+</sup>-induced condensation effect disappearing above 20 mN/m.

There is additionally a shift in the compression moduli of the DPPS monolayer in the presence of both the Ca<sup>2+</sup> and Mg<sup>2+</sup>. The compression modulus was computed from the first derivative of the isotherm in Figure 3C, using the following expression:<sup>89</sup>

$$C^{-1} = -A \frac{d\Pi}{dA} = -A_i \left( \frac{\Pi_{i+1} - \Pi_{i-1}}{A_{i+1} - A_{i-1}} \right) \quad (8).$$

where  $C^{-1}$  is the compression modulus, or inverse compressibility;  $A$  is mean molecular area;  $\Pi$  is surface pressure, and subscript  $i$  represents a particular point along the compression isotherm. In the presence of both the Ca<sup>2+</sup> and Mg<sup>2+</sup>, there is a shift toward higher compression moduli, or lower compressibility, for DPPS (Figure 3D). While the effects on packing appear to diverge between the two ions, similar rigidification of the DPPS



monolayer implies some similarity between Ca-PS and

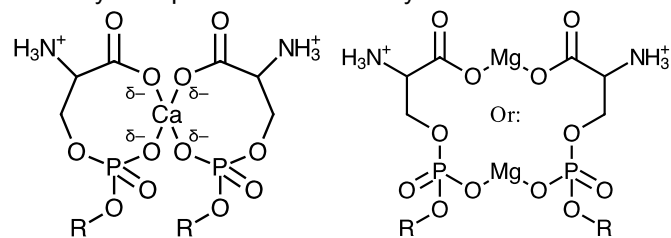


Figure 4: Schematic diagrams comparing (A) the simultaneous bridging of carboxylate and phosphate oxygens by  $\text{Ca}^{2+}$  versus (B)  $\text{Mg}^{2+}$  bridged carboxylate or phosphate regions. These represent the most favourable configurations determined by MD simulations by Martin-Molina et al.<sup>6</sup>

Mg-PS interactions. Analysis of the  $\Pi$ -A isotherms and the compression modulus show a combined condensation and rigidification of the monolayer which is an indication of a binding interaction between  $\text{Ca}^{2+}$  and  $\text{Mg}^{2+}$  with the PS lipids. The mode of the Mg-PS and Ca-PS interactions do not, however, appear identical as the effect of lipid monolayer condensation with  $\text{Ca}^{2+}$  ions is present at all surface pressures, as well as being more pronounced even in the 0 to 20 mN/m region where Mg-induced condensation is seen. Molecular dynamics simulations from Martin-Molina et al. predict a headgroup-bridging effect whereby  $\text{Ca}^{2+}$  and  $\text{Mg}^{2+}$  ions both bind two PS lipids simultaneously.<sup>6</sup> This bridging behavior can explain how both  $\text{Ca}^{2+}$  and  $\text{Mg}^{2+}$  result in higher compressibility, as individual lipids are held more tightly together, which will reduce the ease of deformation. Yet, while both ions were found to bind lipids in a 1:2 ion:lipid ratio, the binding modality was found to be quite different. The most stable conformation of Ca-PS complexation is a motif of four oxygens per  $\text{Ca}^{2+}$  ion, with each lipid coordinating one phosphate oxygen and one carboxylate oxygen to form a cage around the central ion (Figure 4). Conversely, the two most stable forms of the Mg-PS complex were found to involve only two total oxygens, with  $\text{Mg}^{2+}$  bridging either the lipid phosphate or carboxylate regions, but not both simultaneously as calculated for  $\text{Ca}^{2+}$ . These conformations represented the most likely states, though Martin-Molina observed other binding modes at lower probabilities. The average of all possible states found  $\text{Mg}^{2+}$  to bind 2.7 oxygens, while  $\text{Ca}^{2+}$  bound 4.2. Overall,  $\text{Mg}^{2+}$  was found to occupy more superficial positions than  $\text{Ca}^{2+}$ , which penetrated more deeply into the membrane and led to a loss of more associated waters.

The MD simulations by Martin-Molina are consistent with X-ray diffraction studies by Papahadjopoulos which support the conclusions of a larger dehydration effect of  $\text{Ca}^{2+}$  ions on PS.<sup>52</sup> Tighter bridging of the headgroups by  $\text{Ca}^{2+}$  would additionally explain the Ca-induced abolishment of PS lipid phase transition and enhanced fusogenic activity also observed by Papahadjopoulos.<sup>11, 53</sup> These data make clear that while both ions impact the behavior of PS, an overall stronger binding interaction exists between PS and  $\text{Ca}^{2+}$  than with  $\text{Mg}^{2+}$ . SFVS was used to determine whether the binding of either species

results in changes within the C-H stretch or H-bonding regions, which can elucidate how differences in binding modality influence the lipid monolayer structure, both in

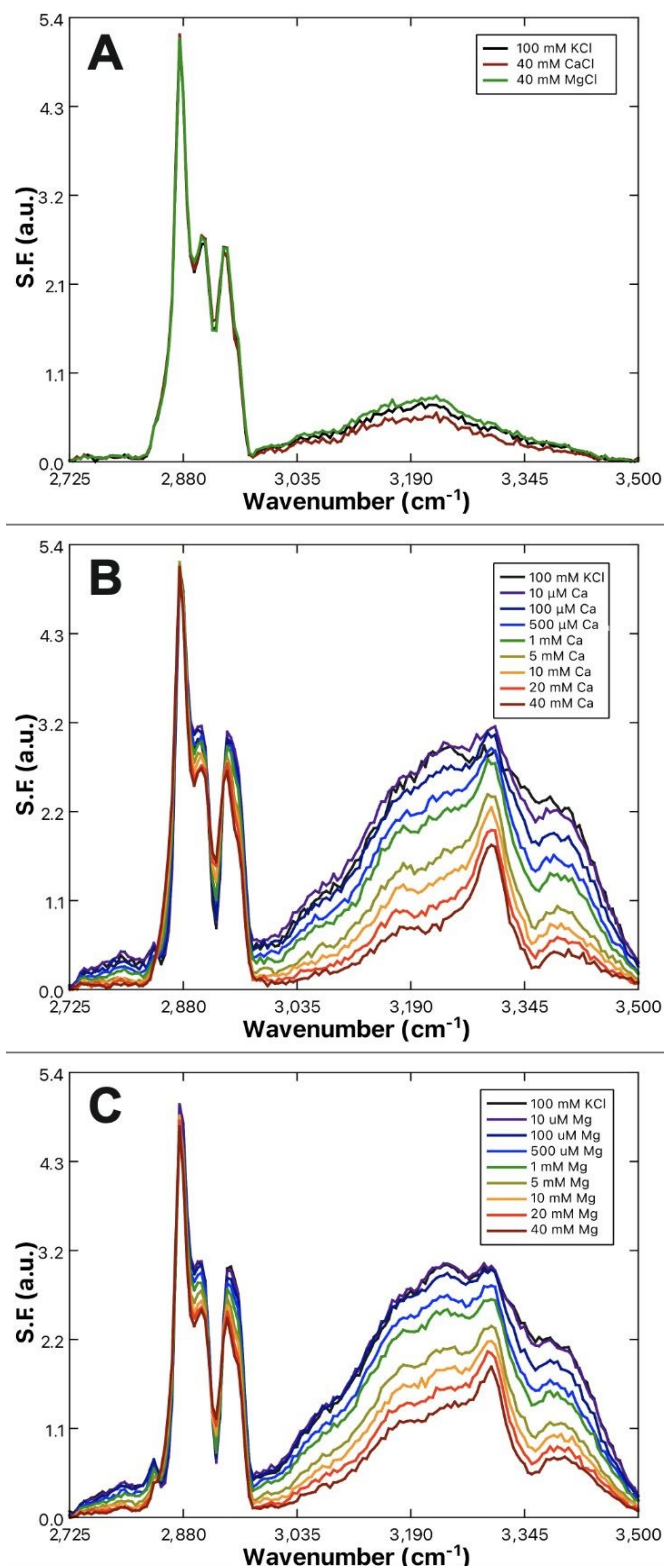


Figure 5: SFVS spectra of hybrid bilayers composed of A) 100% DPPC with 100 mM KCl (black), 40 mM  $\text{CaCl}_2$  (red), and 40 mM  $\text{MgCl}_2$  (green); B) 100% DPPS with increasing concentrations of  $\text{CaCl}_2$ ; C) 100% DPPS with increasing concentrations of  $\text{MgCl}_2$ . All solutions are buffered with Tris at pH 7.4 and maintain a constant ionic strength of 133.4 mM.





terms of tail packing and headgroup solvation.

## Sum-Frequency Analysis

The vibrational spectra of DPPS and DPPC hybrid bilayers were examined to determine whether significant changes to the alkyl chain or hydrogen bonding structure were occurring as a result of  $\text{Ca}^{2+}$  and  $\text{Mg}^{2+}$  binding the DPPS headgroups. The use of hybrid bilayers (lipid monolayers) rather than lipid bilayers is important, as equivalent hydration environments across the bilayer interface would result in interference of sum-frequency generation between the two leaflets. The use of hybrid bilayers removes the antiposed hydration layer associated with headgroups on the opposite leaflet of a symmetric bilayer. Figures 5A-5C illustrate how the SFVS spectra of DPPC and DPPS hybrid bilayers change as a function of  $\text{Ca}^{2+}$  or  $\text{Mg}^{2+}$  concentration. The sum-frequency spectra of these hybrid bilayers can be broken into three general regions of interest: the C-H region from 2800 to 3000  $\text{cm}^{-1}$ , the water region from 3000 to 3500  $\text{cm}^{-1}$ , and an amine peak centered at 3300  $\text{cm}^{-1}$  originating from the hydrogen bonded  $-\text{NH}_3$  group of the PS headgroup. Each of these vibrational features will be analyzed in turn to determine how the structure of the headgroups, associated water layer, and lipid tails respond to bound  $\text{Ca}^{2+}$  and  $\text{Mg}^{2+}$ .

### Amine Peak Analysis

The resonance observed at  $\sim 3300 \text{ cm}^{-1}$  is attributed to the symmetric stretch of the primary amine moiety present on the serine headgroup. The resonance observed here is similar to the sum-frequency spectra obtained from mixtures of ammonia and water, where a 3300  $\text{cm}^{-1}$  band appears due to the ordering of ammonia near the air/water interface.<sup>90</sup> A very prominent 3300  $\text{cm}^{-1}$  also appears within the sum-frequency spectra of fibrinogen-coated surfaces as reported by both the Chen and Cremer groups.<sup>91, 92</sup> Chen and Cremer both attributed the peak to N-H stretches, though disagreed on whether the peak indicated an ordering of the backbone amides (R-NH<sub>2</sub>-R) or side-chain amines (R-NH<sub>3</sub>). Further analysis by Wedner and Castner using a lysine-containing protein analogue LK $\alpha$ 14 supports the hypothesis of the peak being related to the amine groups, as replacement of the lysine nitrogens with <sup>15</sup>N resulted in a shift of the peak.<sup>93</sup> The amine peak, for the purposes of this study, was considered a reporter of the reordering of serine headgroup amines resulting from  $\text{Ca}^{2+}$  or  $\text{Mg}^{2+}$  complexation, in line with the lipid complexing behavior predicted by Martin-Molina et al.<sup>6</sup> as well as phospholipid reorientations observed by Seelig et al.<sup>94</sup>

The amine peak, present only in the PS system, gains in prominence as the bulk  $\text{Ca}^{2+}$  (Figure 5B) or  $\text{Mg}^{2+}$  (Figure 5C) content is increased. The prominence of the amine peak reports directly on structural changes resultant from  $\text{Ca}^{2+}$  or  $\text{Mg}^{2+}$  complexation. Therefore, correlation of the

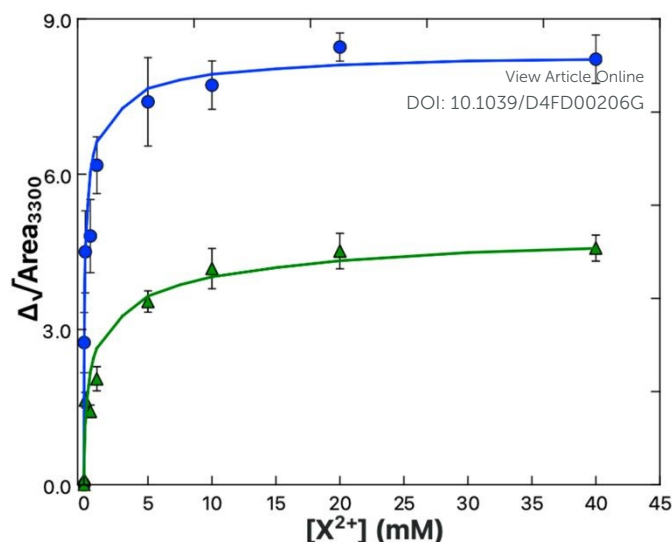


Figure 6: Binding isotherm data for  $\text{Ca}^{2+}$  (blue) and  $\text{Mg}^{2+}$  (green) obtained from the areas of the 3300 $\text{cm}^{-1}$  amine peak in the spectra shown in Figure 5B and 5C respectively. The solid lines are the fits to the data using a Frumkin model (Equation 9).

net area change in the amine peak to the concentration of bulk  $\text{Ca}^{2+}$  or  $\text{Mg}^{2+}$  present was used to derive the binding affinity of  $\text{Ca}^{2+}$  and  $\text{Mg}^{2+}$  to PS by way of a fit to a Frumkin model binding isotherm, Equation 9:<sup>95, 96</sup>

$$A_X \propto \left( \frac{\sqrt{A_{max}K_a[X]}e^{\left(\frac{g'\sqrt{A_X}}{\sqrt{A_{max}}}\right)}}{1 + K_a[X]e^{\left(\frac{g'\sqrt{A_X}}{\sqrt{A_{max}}}\right)}} \right)^2 \quad (9).$$

where  $A_X$  is the amine peak area at a given  $\text{Mg}^{2+}$  or  $\text{Ca}^{2+}$  concentration,  $[X]$ ;  $K_a$  is the binding constant;  $A_{max}$  is the maximum area at surface saturation, and  $g'$  is a constant representing attractive or repulsive forces between binding species. A negative  $g'$  indicates a repulsive interaction, while a positive  $g'$  represents attraction. A  $g'$  of zero results in the standard Langmuir model, which assumes no net interactions of the binding species.

Here it was found that while both  $\text{Ca}^{2+}$  and  $\text{Mg}^{2+}$  bind to the PS monolayer,  $\text{Ca}^{2+}$  will do so with both a higher affinity and a greater impact on the headgroup structure. Figure 6 shows the amine peak area as a function of  $\text{Ca}^{2+}$  and  $\text{Mg}^{2+}$  concentration, with the lines representing the best Frumkin model fit of each dataset to Equation 9. The increase in amine peak area for  $\text{Ca}^{2+}$  is roughly double that of  $\text{Mg}^{2+}$ . A more pronounced ordering of the amines in the case of  $\text{Ca}^{2+}$  is consistent with both the tighter caging of the ion as predicted in Martin-Molina's MD simulations as well as the condensation effect of  $\text{Ca}^{2+}$  on DPPS observed in compression isotherms. The  $K_a$  values of  $1.3 \pm 0.3 \times 10^5$  and  $7.3 \pm 2.5 \times 10^3 \text{ M}^{-1}$  for Ca-PS and Mg-PS, respectively, additionally indicate  $\text{Ca}^{2+}$  ions have around a 20-fold higher affinity toward PS. Newton and Papahadjopoulos reported a 10-fold difference between  $\text{Ca}^{2+}$  and  $\text{Mg}^{2+}$ , roughly matching the order of magnitude relation found here, though their  $K_a$  values of 0.35 and 0.04  $\text{M}^{-1}$  are much



smaller.<sup>52</sup> These values were based on dialysis equilibrium experiments and assumptions were made regarding the permeability and “probable amount of lipid exposed to the bulk solution.” It is possible there was less exposure of the lipids to the Ca<sup>2+</sup> and Mg<sup>2+</sup> solutions than anticipated, which could explain the variance.

An alternate comparison with the results of Hauser et al., who examined Ca-PS affinity via measurement of the surface-enhanced radioactivity of solutions containing <sup>45</sup>Ca in the presence and absence of PS monolayers was also made.<sup>97</sup> Based on increases in surface radioactivity in the presence of PS, representing surface enrichment of Ca relative to the bulk, Hauser determined the Ca-PS affinity to be anywhere from 10<sup>4</sup> to 10<sup>6</sup> M<sup>-1</sup>. Hauser could not go above 1 mM Ca<sup>2+</sup> due to the cost and health concerns related to the use of radioactive isotopes. *K<sub>a</sub>* values were therefore reported as single point measurements not fit to an isotherm model, however the results of Hauser are in relative agreement with the SFVS results. Mg<sup>2+</sup> was not tested by Hauser, so a comparison of relative Mg<sup>2+</sup>/Ca<sup>2+</sup> affinities cannot be made.

Finally, Sinn et al. characterized the binding affinity of PS and Ca<sup>2+</sup> by way of ion selective electrode (ISE) measurements.<sup>98</sup> Known amounts of Ca<sup>2+</sup> were used to titrate a solution containing vesicles composed of 20% DOPS in 80% DOPC. The free concentration of Ca<sup>2+</sup> measured by the probe was compared to the injected amount of Ca<sup>2+</sup> to deduce the amount of Ca<sup>2+</sup> ions bound to the vesicle membranes. Results indicated a binding constant of 650 M<sup>-1</sup>, roughly 200-fold lower than that determined by SFVS. The authors do note however that repeat calibrations of the ISE probe showed drift indicative of lipids depositing to the hydrophobic surfaces of the probe and that the presence of charged lipid on the probe surface could shift the measured Ca<sup>2+</sup> concentration. Sinn et al. hypothesized the lipid coating could either decrease the measured [Ca<sup>2+</sup>] via reduced ion transport across the electrode membrane or increase the measured [Ca<sup>2+</sup>] through electrostatic enrichment in the local Ca<sup>2+</sup> concentration due to the presence of negatively charged PS lipids. The former would increase the determined *K<sub>a</sub>* by reporting an overly large differential in the injected and detected amounts of bulk Ca<sup>2+</sup> whereas the latter would lead to a reduction in the measured *K<sub>a</sub>*. Given Hauser's finding of a great local enrichment of Ca<sup>2+</sup> ions in the presence of PS lipids, it is possible the deviation in results between ISE and SFVS are due to the second scenario put forward by Sinn.

### Water Peak Analysis

The water region from 3000 to 3500 cm<sup>-1</sup> reports on the hydrogen bonding structure within the membrane associated water layer and contains two characteristic water peaks centered at 3200 cm<sup>-1</sup> and 3400 cm<sup>-1</sup>, representing the ice-like O-H symmetric and liquid-like O-H symmetric stretches.<sup>81, 99-101</sup> While both result from the symmetric O-H stretch of water, the ice-like resonance is

indicative of a strong, tetrahedral H-bonding structure like that seen in ice. Conversely, the liquid-like peak results from a weaker H-bonding structure, namely bifurcated H-bonding whereby hydrogens are shared unevenly between neighboring oxygens. It can be seen that the intensity of the water sum-frequency is far higher with DPPS (Figure 5B-C) as compared to DPPC (Figure 5A), results which are in line with previous observations by Allen et al.<sup>102</sup> Allen attributed sum-frequency enhancement in the presence of negatively charged lipids to the ordering of water at the lipid interface, with waters orienting their hydrogens toward the charged lipid headgroups. The observed reduction in water sum-frequency for a DPPS monolayer exposed to either Ca<sup>2+</sup> or Mg<sup>2+</sup> is therefore hypothesized to result from neutralization of membrane surface charge and relaxation of the electrostatically imposed ordering of water. Conversely, the lack of an increase in sum-frequency from the water region of the DPPC hybrid bilayer when exposed to Ca<sup>2+</sup> or Mg<sup>2+</sup> ions implies the neutral DPPC lipids have not increased in charge. It is therefore hypothesized that either no binding of Ca<sup>2+</sup> or Mg<sup>2+</sup> has occurred, or that any bound Ca<sup>2+</sup> and Mg<sup>2+</sup> simply displace previously bound Na<sup>+</sup> ions in a surface charge conserving manner. Both the hypothesized rationales for the DPPS and DPPC sum-frequency water band responses to Ca<sup>2+</sup> or Mg<sup>2+</sup> rely upon the interpretation that sum-frequency in the water region is sensitive to the charge state of the lipids.

The influence of interfacial charge on the observed sum-frequency intensity has been previously considered by others as a third order,  $\chi^{(3)}$  effect.<sup>103-110</sup> Just as the  $\chi^{(2)}$  tensor describes a material's response to the coupling of two incident electric fields, the  $\chi^{(3)}$  tensor describes a material's response to three incident fields. In the present case, two are the  $E_{532}$  and  $E_{IR}$  from the incoming 532 nm and IR beams and the third is a static field,  $E_{DC}$ , which is produced by the charged DPPS/water interface. The total sum-frequency generated is expressed as a summation of the respective second and third order contributions:<sup>105-108, 110-113</sup>

$$I_{SF} \propto |\chi^{(2)} + \chi^{(3)}E_{DC}|E_{IR}E_{532}|^2 \quad (10).$$

Depending on the material properties,  $E_{DC}$  may influence  $\chi^{(3)}$  in various ways. As noted by Allen, Eisenthal, Levine and others, dipolar molecules, like water, will realign within a static electric field.<sup>100, 102, 105-107, 110, 114</sup> As  $\chi^{(2)}$  depends on the molecular axis being probed, realignment of interfacial molecules can yield changes in sum-frequency generation without necessarily resulting directly from third-order coupling. Therefore, the static field ( $E_{DC}$ ) contributions can be expressed as a summation of two components, one dependent on third-order molecular hyperpolarizability ( $\gamma$ ) and the other dependent on molecular rearrangement of the second-order molecular hyperpolarizability ( $\beta$ ).  $\chi^{(3)}$  can then be expressed as:<sup>105-107</sup>



$$\chi^{(3)} = N^{(3)}\gamma + \frac{\mu N^{(2)}\beta}{5k_B T} \quad (11).$$

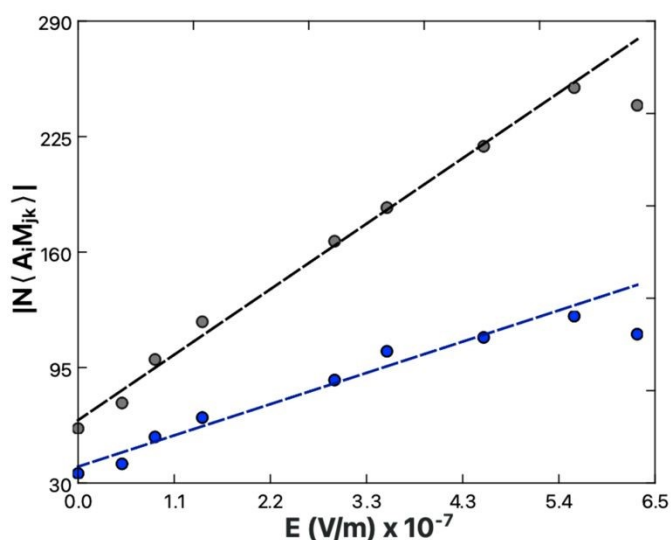


Figure 7: 3200  $\text{cm}^{-1}$  (black) and 3400  $\text{cm}^{-1}$  (blue) peak transition probabilities from spectral fits of Ca-exposed DPPS (Figure 5B) plotted as a function of the electric field strength one Debye length away from the lipid surface (Table 1). The determined slopes, representing the relative  $\chi^{(3)}$ , are  $3.4 \pm 0.1 \times 10^6 \text{ m/V}$  for the ice-like 3200  $\text{cm}^{-1}$  and  $1.6 \pm 0.1 \times 10^6$  for the water-like 3400  $\text{cm}^{-1}$ .

where  $N^{(3)}$  is volumetric number density in molecules per  $\text{cm}^3$ ,  $N^{(2)}$  is the surface density in molecules per  $\text{cm}^2$ ,  $\mu$  is the dipole moment of the molecules,  $k_B$  is Boltzmann constant, and  $T$  is temperature in Kelvin. In cases where  $\mu$  is large, molecular alignment within an applied  $E_{DC}$  field will magnify  $\chi^{(3)}$  through the  $\frac{\mu N^{(2)}\beta}{5k_B T}$  term.<sup>107, 110</sup> Substitution of Equation 11 into Equation 10 yields the relationship between the generated sum-frequency and  $E_{DC}$  field strength:

$$I_{SF} \propto \left| \left( \chi^{(2)} + \left[ N^{(3)}\gamma + \frac{\mu N^{(2)}\beta}{5k_B T} \right] E_{DC} \right) E_{IR} E_{532} \right|^2 \quad (12).$$

The magnitude of the static  $E_{DC}$  field is itself ultimately determined by the surface charge density and the ionic strength of solution. The surface charge will generate a surface potential in accordance with Equation 13:<sup>9, 14, 115-117</sup>

$$\phi_0 = \frac{2k_B T}{e} \sinh^{-1} \left( \frac{\sigma}{\sqrt{8000k_B T N_A I \epsilon_0 \epsilon_r}} \right) \quad (13).$$

where  $\phi_0$  is the surface potential;  $\sigma$  is the surface charge density in  $\text{C/m}^2$ ;  $I$  is the ionic strength of solution in molarity;  $N_A$  is Avogadro's number;  $\epsilon_0$  is the vacuum permittivity; and  $\epsilon_r$  is the relative permittivity of the medium.<sup>9, 14, 115-117</sup> Gouy-Chapman theory predicts that the surface potential decays with distance away from the interface, with the effective potential at any given distance described by:

$$\phi_x = \phi_0 e^{-\kappa x} \quad (14).$$

where  $x$  is distance from the charged surface and  $\kappa$  is the inverse Debye screening length.<sup>118</sup> The  $E_{DC}$  field strength is taken to be the rate of change, or derivative, of the potential at one Debye length from the surface:

$$E_{DC} = \frac{d\phi_x}{dx} \text{ at } \kappa^{-1} = -\kappa\phi_0 e^{-\kappa\kappa^{-1}} = -\kappa\phi_0 e^{-1} \quad (15).$$

The charge density of the DPPS membrane was computed using the MMA of the DPPS monolayer obtained from the pressure-area isotherms. Given a mean molecular area of  $49.3 \pm 0.5 \text{ \AA}^2$  for DPPS at a deposition pressure of 30  $\text{mN/m}$ , the theoretical maximum charge density for a pure DPPS monolayer is  $-0.33 \text{ C/m}^2$ . Conversely, at a saturating concentration of Ca, one would expect the PS lipids to have a charge state of zero, assuming a binding ratio of 2:1 PS:Ca. Using these surface charge limits and the isotherm data in Figure 6, Table 1 lists the surface saturation, charge density ( $\sigma$ ), surface potential ( $\phi_0$ ), and electric field strength one Debye length away from the surface ( $E_{\kappa^{-1}}$ ) for each bulk concentration of  $\text{Ca}^{2+}$ . The Debye length for all calculations was taken to be 0.828 nm as the ionic strength was held constant at 133.4 mM.

Table 1: Calculation of electric field strengths using the predicted surface charge densities from Equations 14 & 15. Ionic strength was held constant at 133.4 mM, with a Debye length of 0.828 nm. The percent surface saturation of  $\text{Ca}^{2+}$  is taken from the amine peak binding isotherm (Figure 6).

[Ca] (mM)	$\Gamma_{\text{Ca}^{2+}}$	$\frac{\sigma_i}{\sigma_{\text{max}}}$	$\sigma_i$ ( $\text{Cm}^{-2}$ )	$\phi_0$ (V)	$E_{DC}$ ( $\text{V/m}) \times 10^{-7}$
0	0	100%	-0.33	-0.142	6.30
0.01	27%	73%	-0.25	-0.126	5.59
0.1	54%	46%	-0.16	-0.103	4.57
0.5	72%	28%	-0.094	-0.078	3.48
1	79%	21%	-0.070	-0.065	2.89
5	92%	8%	-0.028	-0.031	1.40
10	95%	5%	-0.017	-0.020	8.67
20	97%	3%	-0.009	-0.010	4.95
40	100%	0%	0	0	0

The validity of the calculated surface saturation and surface charge density values were evaluated as follows. The spectra of Figure 5B were fit using Equation 4 to obtain the transition probability amplitudes [ $PA = (N\langle A_i M_j k \rangle)$ ] for the ice-like 3200  $\text{cm}^{-1}$  and water-like 3400  $\text{cm}^{-1}$  resonances. Equating Equation 4 and Equation 12 at a specific resonance yields:

$$PA \propto \left| \left( \chi^{(2)} + \left[ N^{(3)}\gamma + \frac{\mu N^{(2)}\beta}{5k_B T} \right] E_{DC} \right) \right| \quad (16).$$

from Equation 16,  $PA$  is expected to scale linearly with  $E_{DC}$ . Figure 7 shows the relationship between the calculated  $E_{DC}$  and observed transition probabilities of the ice-like (3200  $\text{cm}^{-1}$ ) and water-like (3400  $\text{cm}^{-1}$ ) peaks, respectively. A linear relationship between  $E_{DC}$  for both the ice-like and



water-like peak amplitudes is observed which, firstly, confirms  $E_{DC}$  scaling of  $\chi^{(3)}$  for the DPPS associated water layer. Secondly, these data also validate the use of the 3300  $\text{cm}^{-1}$  amine peak as a gauge of  $\text{Ca}^{2+}$  adsorption and the associated membrane charge density. The starting assumption stipulated that the amine peak resulted from reorientation of the amines on the serine headgroup due to a 2:1 PS:Ca complexation. Under such a motif, the  $E_{DC}$  should be reduced due to charge neutralization of PS upon binding  $\text{Ca}^{2+}$ . A linear drop in the ice- and water-like transition probabilities with respect to  $E_{DC}$  supports these previous assumptions. There does, however, seem to be a deviation from linearity beyond an  $E_{DC}$  of  $5.59 \times 10^7$  V/m. The 10  $\mu\text{M}$   $\text{Ca}^{2+}$  and zero  $\text{Ca}^{2+}$  data have roughly equal water intensity despite the binding isotherm predicting around 27% neutralization of the surface charge should have occurred. The deviation from linearity seen in Figure 7 is explained by considering the two types of contributions to  $\chi^{(3)}$  detailed in Equation 11. As observed by both Richmond and Kielich,  $E_{DC}$  scaling reaches a saturation point beyond which there is no further change in intensity.<sup>99, 110</sup> Saturation occurs in instances where  $\chi^{(3)}$  has significant contributions from molecular reorientations,  $(\frac{\mu N^{(2)}\beta}{5k_B T})$ , as opposed to being purely third-order coupling,  $(N^{(3)}\gamma)$ . Both Richmond and Kielich attributed saturation to a limit on the alignment of the interfacial water within the  $E_{DC}$  field.<sup>99, 110</sup> Once the  $E_{DC}$  strength is sufficient to orient the water dipoles along the  $E_{DC}$  field vector, further increases in field strength will not yield further alignment. The realignment term,  $\frac{\mu N^{(2)}\beta}{5k_B T}$ , is thus maximized and higher  $E_{DC}$  fields further magnify only the  $N^{(3)}\gamma$  component of  $\chi^{(3)}$ . The deviation seen here is therefore ascribed to maximal water alignment beyond  $E_{DC} = 5.59 \times 10^7$  V/m. Accordingly, the line fits of Figure 7 were limited to the linear region.

The ice-like peak results from tightly ordered water structures, whereas the water-like peak results from more transient and disordered H-bonding. As previously detailed by Gragson and Richmond, application of an electric field will lead to sequential conversion of disordered bulk water to the semi-ordered population resonant at 3400  $\text{cm}^{-1}$  and from the semi-ordered population to the tetrahedrally ordered population resonant at 3200  $\text{cm}^{-1}$ .<sup>99</sup> Gragson and Richmond altered the  $E_{DC}$  field strength through modulation of either the density of charged sodium dodecyl sulfate (SDS) molecules at the air/water interface or the bulk ionic strength. In both cases it was found the 3200  $\text{cm}^{-1}$  peak responded more strongly to the electric field due to population migration of water molecules toward the more ordered state.

The rate of change of the ice-like and water-like amplitudes  $[N(A_i M_{jk})]$ , with respect to  $E_{DC}$  were used to examine the relative  $\chi^{(3)}$  of each peak. In Figure 7, the  $\chi^{(3)}$  for the ice-like and water-like peaks is represented by the slope of each line (Equation 10). The data yield  $\chi^{(3)}$  values of  $3.4 \pm 0.1 \times 10^6$  m/V for the ice-like 3200  $\text{cm}^{-1}$  and  $1.6 \pm 0.1 \times 10^6$  m/V for the water-like 3400  $\text{cm}^{-1}$ . The relative ice-like to water-like

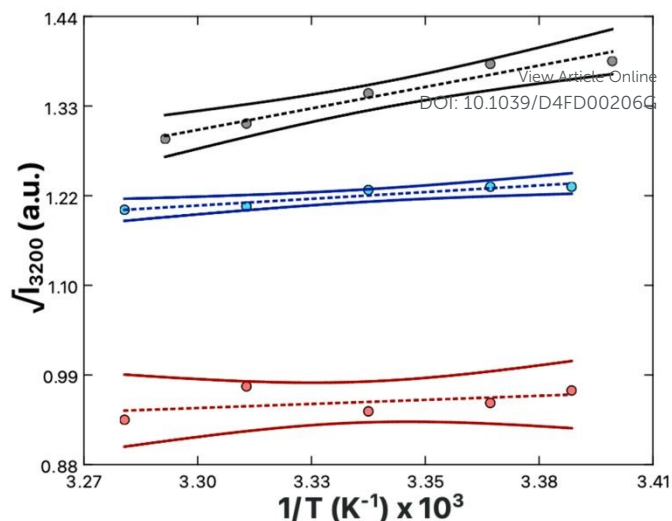


Figure 8: Square root of SFVS intensity measured at 3200  $\text{cm}^{-1}$  for a hybrid DPPS bilayer as a function of inverse temperature. The data were collected at concentrations of: 100 mM KCl + zero  $\text{CaCl}_2$  (black), 97 mM KCl + 1 mM  $\text{CaCl}_2$  (blue), and 40 mM Ca (red). The dashed lines are the linear fits to the data. The solid lines indicate the 95% confidence intervals for each linear regression. All solutions were buffered with Tris at pH 7.4 and maintain a constant ionic strength of 133.4 mM.

$\chi^{(3)}$  ratio is thus found to be  $2.1 \pm 0.1$ . A larger  $\chi^{(3)}$  for the 3200  $\text{cm}^{-1}$  peak is in agreement with Gragson and Richmond's findings of net population conversion of water molecules toward the more ordered ice-like state at higher  $E_{DC}$ . As the water population conversion requires reordering of the water molecules, it is concluded  $E_{DC}$  dependent molecular rearrangements are occurring within the solvation layer. These data are limited, however, in that while the presence of molecular rearrangement is suggested, the magnitude of  $\frac{\mu N^{(2)}\beta}{5k_B T}$  relative to the static component,  $N^{(3)}\gamma$ , of  $\chi^{(3)}$  remains unclear.

The relative magnitude of the molecular rearrangement and third-order contributions was assessed as follows. From Equation 12, only the molecular rearrangement term,  $\frac{\mu N^{(2)}\beta}{5k_B T}$ , of  $\chi^{(3)}$  has a  $1/T$  dependence. Determination of the relative contributions of the dynamic and static components of  $\chi^{(3)}$ ,  $\frac{\mu N^{(2)}\beta}{5k_B T}$  and  $N^{(3)}\gamma$ , respectively, was therefore performed by measurement of the sum-frequency intensity as a function of  $1/T$  for the 3200  $\text{cm}^{-1}$  ice-like peak, Figure 8.<sup>105, 106</sup> The ice-like resonance was chosen due to its larger  $\chi^{(3)}$ , as found in Figure 7. A linear relationship between the the square root of the sum-frequency intensity and  $1/T$  should be observed if  $E_{DC}$  induced reorganization of water is occurring,<sup>105</sup> with the slope and intercept terms equal to:

$$\text{Slope} = \frac{\mu N\beta}{5k_B} E_{DC} E_{IR} \quad (17).$$

$$\text{Intercept} = (\chi^{(2)} + N^{(3)}\gamma E_{DC}) E_{532} E_{IR} \quad (18).$$

The relative influences of the dynamic realignment,  $\frac{\mu N^{(2)}\beta}{5k_B T}$ , and static third-order,  $N^{(3)}\gamma$ , contributions to  $\chi^{(3)}$



were calculated as follows. Intensity data was collected in the absence of  $\text{Ca}^{2+}$ , as well as in the presence of 1 mM  $\text{Ca}^{2+}$  or 40 mM  $\text{Ca}^{2+}$ . These data contain three important trends. Firstly, a linear trend is observed in the zero and 1mM  $\text{Ca}^{2+}$  systems. As the realignment contribution,  $\frac{\mu N^{(2)}\beta}{5k_B T}$ , is the only temperature dependent term in Equation 12, the results validate the hypothesis of electrostatically induced water reorganization. Secondly, it is shown the  $1/T$  dependence decreases as the concentration of  $\text{Ca}^{2+}$  increases. As per Equation 17, the slope, representing the dynamic term  $\frac{\mu N^{(2)}\beta}{5k_B T}$ , is scaled by  $E_{DC}$ . Observation of reduced  $E_{DC}$  as  $\text{Ca}^{2+}$  content is increased is further evidence of charge neutralization of PS lipids as  $\text{Ca}^{2+}$  binds. Lastly, at 40 mM  $\text{Ca}^{2+}$  the slope of the line becomes indistinct from zero ( $180 \pm 200$ ). The conclusion is that complete neutralization of PS headgroup charges has occurred resulting in  $E_{DC} = 0$ . Complete neutralization supports the previous assumption of a 2:1 PS: $\text{Ca}^{2+}$  binding ratio. Further, the neutralization point agrees with the amine peak-derived binding isotherm (Figure 6), which indicates surface saturation at 40 mM  $\text{Ca}^{2+}$ .

From the previous analysis, it becomes possible to determine the relative contributions (Equation 12) to  $\chi^{(3)}$ . The contribution from molecular rearrangements,  $\frac{\mu N^{(2)}\beta}{5k_B T}$ , at any temperature  $T$  is simply the product of the measured slope and  $1/T$  (Equation 17). As all sum-frequency spectra shown in Figures 5A-5C were collected at 21 °C,  $T = 294.15$  K is used here. The determined slopes of  $960 \pm 130$  K and  $300 \pm 60$  K yield  $\frac{\mu N^{(2)}\beta}{5k_B T}$  values of  $3.26 \pm 0.44$  and  $1.02 \pm 0.35$  for the zero  $\text{Ca}^{2+}$  and 1 mM  $\text{Ca}^{2+}$  data, respectively. The static third-order contributions,  $N^{(3)}\gamma$ , can be determined from rearrangement of Equation 18. To accomplish this, however, the value of  $\chi^{(2)}$  must be known.  $\chi^{(2)}$  is obtained from the 40 mM  $\text{Ca}^{2+}$  data set, as complete neutralization of surface charge results in an  $E_{DC}$  of zero. The average of all the measured  $3200 \text{ cm}^{-1}$  sum-frequency intensities at 40 mM  $\text{Ca}^{2+}$  yields a relative  $\chi^{(2)}$  of  $0.958 \pm 0.008$ . Using this  $\chi^{(2)}$  value, the static third-order contributions,  $N^{(3)}\gamma$ , were calculated for the zero  $\text{Ca}^{2+}$  and 1 mM  $\text{Ca}^{2+}$  systems. From the determined intercepts of  $-1.85 \pm 0.42$  and  $0.21 \pm 0.21$ ,  $N^{(3)}\gamma$  values of  $-2.81 \pm 0.43$  and  $-0.75 \pm 0.22$  are obtained for the zero  $\text{Ca}^{2+}$  and 1 mM  $\text{Ca}^{2+}$  data, respectively. The relative contribution of dynamic realignment ( $\frac{\mu N^{(2)}\beta}{5k_B T}$ ) to  $\chi^{(3)}$  is therefore  $54 \pm 9\%$  and  $57 \pm 8\%$  for the zero  $\text{Ca}^{2+}$  and 1 mM  $\text{Ca}^{2+}$  data, respectively. The results suggest an equal contribution of the dynamic and static components to  $\chi^{(3)}$ , within error. At saturation, where maximum dipole alignment and maximum  $\frac{\mu N^{(2)}\beta}{5k_B T}$  is reached, further increases in  $E_{DC}$  are predicted to increase the contribution from the negative  $N^{(3)}\gamma$  term while contributions from  $\frac{\mu N^{(2)}\beta}{5k_B T}$  would remain constant. Increases in  $E_{DC}$  beyond saturation are therefore expected to reduce the total  $\chi^{(3)}$  and result in a drop in generated sum-frequency. From Figure 7 it can be seen

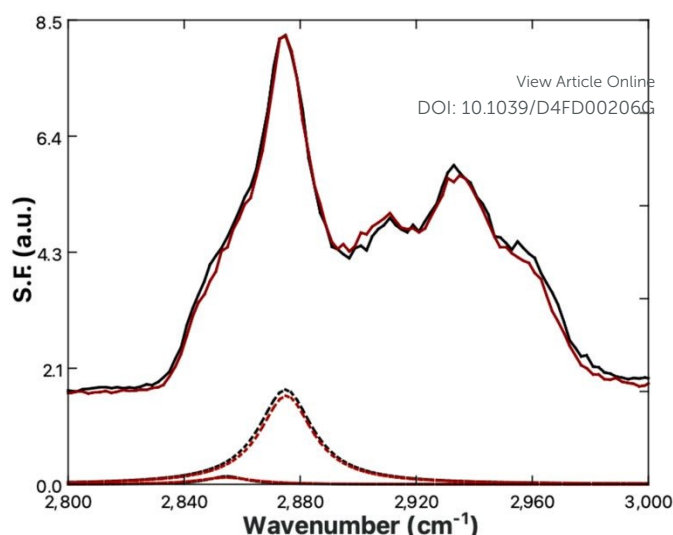


Figure 9: SFVS spectra of DPPS in  $\text{D}_2\text{O}$  with 100 mM KCl (black) or 40 mM  $\text{CaCl}_2$  (red). The offset curves (dashed lines) are the spectral fits of the  $\text{CH}_2 \nu_s$  and  $\text{CH}_3 \nu_s$  peaks at  $2850 \text{ cm}^{-1}$  and  $2875 \text{ cm}^{-1}$  respectively obtained using Equation 4. All solutions were buffered with Tris at pH = 7.4 with a total ionic strength of 133.4 mM. Spectra were recorded at  $21^\circ\text{C}$

that maximum  $3200 \text{ cm}^{-1}$  amplitude is reached at  $5.59 \times 10^7 \text{ V/m}$ , which then decreases at  $6.30 \times 10^7 \text{ V/m}$ . These data are consistent with maximal water alignment at  $5.59 \times 10^7 \text{ V/m}$ .

#### Alkyl Chain Analysis

The alkyl chain C-H stretches, found between 2800 and  $3000 \text{ cm}^{-1}$ , were characterized to determine whether the lipid tails undergo any structural changes as PS binds  $\text{Ca}^{2+}$  or  $\text{Mg}^{2+}$ . All five peaks previously detailed for the bilayer system of Figure 1 are present, with an additional peak at  $2920 \text{ cm}^{-1}$  due to the  $\text{CH}_3$  symmetric stretch of the methylated surface. The C-H region of the DPPC system in Figure 5A displays no change when comparing the 100 mM KCl, 40 mM  $\text{CaCl}_2$ , and 40 mM  $\text{MgCl}_2$  solutions. Conversely, changes are quite apparent within the C-H bands of DPPS as  $\text{Ca}^{2+}$  (Figure 5B) or  $\text{Mg}^{2+}$  (Figure 5C) content is increased. At first glance this may imply an alteration in the packing structure of the lipid tails; however, the C-H region of the DPPS sits atop the trailing edge of the water stretches, the magnitudes of which are highly influenced by both  $\text{Ca}^{2+}$  and  $\text{Mg}^{2+}$  association due to charge screening.

The direct effect of  $\text{Ca}^{2+}$  ions on DPPS tail structure was determined by isolation of the C-H region from the water region. SFSV spectra were recorded in buffered  $\text{D}_2\text{O}$  to remove the water features from the spectra. Figure 9 illustrates the influence  $\text{Ca}^{2+}$  has on the C-H region, absent any O-H bands. Comparing the 100 mM KCl (zero  $\text{Ca}^{2+}$ ) and 40 mM  $\text{Ca}^{2+}$  solutions, it is clear the changes observed in Figure 5B are not due to changes in the C-H bands intensities, but rather result from  $\text{Ca}^{2+}$  induced disruption of the underlying water resonance.

The ratio of the  $\text{CH}_2$  symmetric stretch ( $\nu_s$ ) at  $2850 \text{ cm}^{-1}$  and the  $\text{CH}_3 \nu_s$  at  $2875 \text{ cm}^{-1}$  has previously been used to



evaluate net changes in gauche content within the chain structure.<sup>82, 119-122</sup> Increased ordering of the alkyl chains is expected to result in reduced gauche content, which is observed in sum-frequency spectra as reduced CH<sub>2</sub> v<sub>s</sub> character relative to the CH<sub>3</sub> v<sub>s</sub> due to cancelation of sum-frequency within the locally symmetric trans configuration.<sup>80, 119, 120</sup> Ordering of the alkyl chains from Ca<sup>2+</sup> induced condensation of DPPS would be expected to result in a decrease in the CH<sub>2</sub> v<sub>s</sub> to CH<sub>3</sub> v<sub>s</sub> peak ratio. The sum-frequency spectra of Figure 9 were fit using Equation 4 to calculate the CH<sub>2</sub>:CH<sub>3</sub> ratio for the 100 mM KCl and 40 mM CaCl<sub>2</sub> data, which remains unchanged within error at 0.20 ± 0.05 and 0.17 ± 0.06, respectively. The observed invariance of the CH<sub>2</sub>:CH<sub>3</sub> ratio with respect to Ca<sup>2+</sup> induced condensation of DPPS is taken to simply be a result of minimal initial gauche content within the alkyl chains. The membranes under measurement here were deposited at 30 mN/m, within the gel phase where gauche content of saturated lipids is expected to be minimal, for example H<sup>1</sup>NMR and FT-IR analysis place the gauche vs trans conformation of DPPC at less than 3%.<sup>123, 124</sup> Given DPPS has the same 16-carbon alkyl chain lengths as DPPC, a similarly low gauche content would be expected.

### Flip-flop Kinetics

The central hypothesis of the current work is that PS expression can be influenced by Ca<sup>2+</sup>. At equilibrium, a net population difference in the number density of PS lipids is possible if the rate constants for PS flip and flop are not equal:

$$\frac{k_{flip}}{k_{flop}} = \frac{N_{proximal}}{N_{distal}} \quad (19).$$

To achieve this, Ca<sup>2+</sup> ions need to alter the flip-flop mixing behavior of PS lipids such that PS lipids will flip and flop at different rates in the presence and absence of Ca<sup>2+</sup>. To test the hypothesis, DPPS flip-flop kinetics of asymmetric PSLBs containing physiologic levels of 10% PS were performed to determine if the binding interactions observed between PS and Ca<sup>2+</sup> or Mg<sup>2+</sup> affect the rate of DPPS flip-flop. The concentration of Ca<sup>2+</sup> and Mg<sup>2+</sup> were 1 mM to mimic the physiologic concentrations of the extracellular fluid and cytosol, respectively.<sup>55, 56</sup> KCl controls without Ca<sup>2+</sup> or Mg<sup>2+</sup> were also collected as a baseline for comparison. Figures 10A-10C show representative DPPS flip-flop decays for both DPPC and DPPS with Ca<sup>2+</sup> or Mg<sup>2+</sup>, while Figures 10D and 10E show linearized Eyring plots of all determined flip-flop rates.

Eyring plots were generated from the Eyring equation, which relates the rate of flip-flop,  $k$ , to the transition state free energy,  $\Delta G^\ddagger$ .<sup>64, 67, 125</sup>

$$\frac{hk}{k_B T} = e^{\frac{\Delta G^\ddagger}{RT}} \quad (20).$$

where  $h$  is Planck's constant,  $k_B$  is Boltzmann's constant,  $R$  is the molar gas constant, and  $T$  is temperature in Kelvin. In the linearized form, the Eyring relation is expressed as:

$$\ln\left(\frac{k}{T}\right) = \ln\left(\frac{k_B}{h}\right) - \frac{\Delta G^\ddagger}{RT} \quad (21).$$

which allows for linear presentation of all kinetic data as well as determination of the change in the transition state free energy of flip-flop due to DPPS or DPPC lipids binding Ca<sup>2+</sup> or Mg<sup>2+</sup> ions.

Considering the DPPC controls first, no effect of Mg<sup>2+</sup> or Ca<sup>2+</sup> on the rate of DPPC flip-flop was observed. A representative comparison of DPPC flip-flop behavior is shown in Figure 10A, where the rate of DPPC flip-flop is found to be 3.35 ± 0.03 × 10<sup>-5</sup> s<sup>-1</sup> at 26.9 °C or 3.45 ± 0.04 × 10<sup>-5</sup> s<sup>-1</sup> at 26.6 °C in the presence and absence of 1 mM Ca<sup>2+</sup>, respectively. The slight deviation in rate is considered within experimental variance as, from Figure 10D, the 95% confidence intervals of the DPPC flip-flop rates in the presence and absence of 1 mM Ca<sup>2+</sup> overlap. Likewise, measured flip-flop rates for DPPC in the presence of 1 mM Mg<sup>2+</sup> fall within the 95% confidence intervals for DPPC flip-flop rates both in the presence and absence of 1 mM Ca<sup>2+</sup>. The lack of any influence of Ca<sup>2+</sup> or Mg<sup>2+</sup> on DPPC flip-flop rates is in agreement with the compression isotherms which found no change in the MMA in the presence of Ca<sup>2+</sup> or Mg<sup>2+</sup>, results which indicate neither ion had bound DPPC. Likewise, bound Ca<sup>2+</sup> or Mg<sup>2+</sup> would be expected to increase the surface charge density of the neutral DPPC lipids and, through  $\chi^{(3)}$  (Equation 13), scale the sum-frequency generated by the 3200 cm<sup>-1</sup> and 3400 cm<sup>-1</sup> water peaks. No such effect was observed in sum-frequency scans of DPPC hybrid bilayers in the presence and absence of Ca<sup>2+</sup> or Mg<sup>2+</sup> (Figure 5A). The sum-frequency spectra, compression isotherms, and flip-flop data are all consistent with no observable binding interaction between the PC headgroup and either Ca<sup>2+</sup> or Mg<sup>2+</sup>.

Determination of the flip-flop kinetics for 10% DPPS + 90% DPPC membranes was performed with respect to both the DPPS and DPPC fractions. The effect of 10% DPPS on the parent DPPC matrix was examined by measurement of the flip-flop rate of 90% DPPC in the presence of 10% DPPS with 1 mM Ca<sup>2+</sup> (87.3% DPPC + 9.7% DPPSd62 + 3% PEG5000-PE / 90% DPPCd62 + 10% DPPSd62, proximal/distal). The flip-flop rates fall within the 95% confidence intervals of the flip-flop rates obtained for a pure DPPC membrane shown in Figure 10D. This result indicates that the presence of 10 mol% DPPS has no influence on DPPC flip-flop. The flip-flop behavior of the PS fraction, however, yields more interesting results. The rate of DPPS flip-flop in DPPC (87.3% DPPCd62 + 9.7% DPPS + 3% PEG5000-PE / 90% DPPCd62 + 10% DPPSd62, proximal/distal) show a pronounced effect of Ca<sup>2+</sup> on the rate of DPPS flip-flop. The rate of DPPS flip-flop decreased from 7.11 ± 0.08 × 10<sup>-5</sup> s<sup>-1</sup> (24.7 °C) in the



absence of  $\text{Ca}^{2+}$  to  $1.46 \pm 0.07 \times 10^{-5} \text{ s}^{-1}$  (24.5 °C) when in the presence of 1 mM  $\text{Ca}^{2+}$ , roughly a 5-fold decrease. Alternatively, Figure 10C shows a comparison of DPPS flip-flop measured in the presence of 1 mM  $\text{Mg}^{2+}$  at 24.5 °C compared to DPPS flip-flop in the absence of  $\text{Ca}^{2+}$  or  $\text{Mg}^{2+}$  at 24.7 °C (same as Figure 10B). The measured flip-flop rate of  $6.8 \pm 0.1 \times 10^{-5} \text{ s}^{-1}$  for the 1 mM  $\text{Mg}^{2+}$  exposed DPPS is essentially identical to the  $7.11 \pm 0.08 \times 10^{-5} \text{ s}^{-1}$  flip-flop rate measured in the absence of  $\text{Mg}^{2+}$ . All flip-flop rates measured for DPPS in the presence of 1 mM  $\text{Mg}^{2+}$  fall within the 95% confidence intervals of DPPS flip-flop in the absence of  $\text{Ca}^{2+}$  or  $\text{Mg}^{2+}$ , whereas all flip-flop rates measured for DPPS in the presence of 1 mM  $\text{Ca}^{2+}$  fall outside (Figure 10E).  $\text{Ca}^{2+}$  exposure has a pronounced and specific slowing effect on DPPS translocation. From Equation 19, the slowed flip-flop kinetics of DPPS in the presence of  $\text{Ca}^{2+}$  (Figure 10B) results from an increase in  $\Delta G^\ddagger$  from  $96.6 \pm 0.1 \text{ kJ/mol}$  in the absence of  $\text{Ca}^{2+}$  to  $100.5 \pm 0.2 \text{ kJ/mol}$  in the presence of 1 mM  $\text{Ca}^{2+}$ , an increase of  $3.9 \pm 0.2 \text{ kJ/mol}$ . In the presence of 1 mM  $\text{Mg}^{2+}$ , the  $\Delta G^\ddagger$  of  $96.7 \pm 0.2 \text{ kJ/mol}$  remains within error of the  $\Delta G^\ddagger$  in the absence of  $\text{Ca}^{2+}$  or  $\text{Mg}^{2+}$ .

The divergence in DPPS response to the presence of

$\text{Ca}^{2+}$  and  $\text{Mg}^{2+}$  can be attributed to two important factors. Firstly,  $\text{Mg}^{2+}$  was found to have a PS binding affinity roughly 20-fold lower than  $\text{Ca}^{2+}$ . Yet further, the binding data from Figure 6 shows bound  $\text{Mg}^{2+}$  does not produce as great of an impact on the ordering of the serine headgroup amines. A 1 mM concentration of  $\text{Mg}^{2+}$  resulted in an amine peak area increase roughly equivalent to just 10  $\mu\text{M}$   $\text{Ca}^{2+}$ . These results track well with Papahadjopoulos, who observed a 10-fold differential in  $\text{Ca}^{2+}$  and  $\text{Mg}^{2+}$  binding affinity, and noted only  $\text{Ca}^{2+}$  lead to fusion of PS-containing vesicles or phase segregation of PS.<sup>11, 51-54</sup>  $\text{Mg}^{2+}$  ions have lower PS affinity, more muted impact on headgroup structure, and lower denticity binding to the membrane as predicted by MD simulations,<sup>6</sup> and it is therefore not surprising to find that  $\text{Mg}^{2+}$ 's binding modality is simply too weak to influence translocation.

$\text{Ca}^{2+}$  has a unique ability to slow the rate of DPPS translocation relative to  $\text{Mg}^{2+}$ , which has no measurable effect. The finding has potentially important implications for PS expression *in vivo*. The extracellular concentration of  $\text{Ca}^{2+}$  is far higher than within the cytosol, at 1 mM and 100 nM, respectively.<sup>56</sup> Some degree of  $\text{Ca}^{2+}$  induced PS externalization could therefore be explained in terms of the

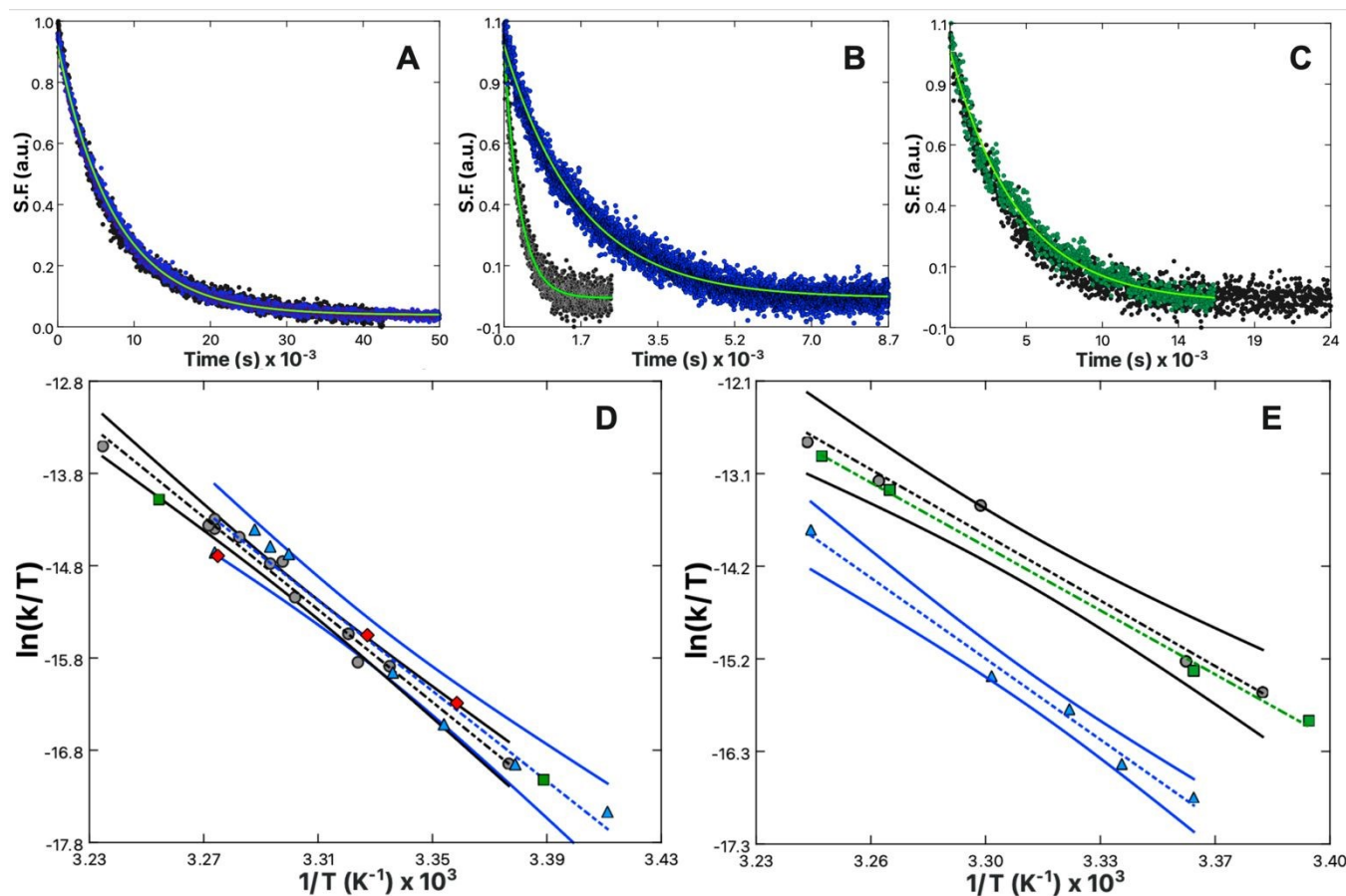


Figure 10: Representative SFVS intensity decays of the  $\text{CH}_3$  symmetric stretch at  $2875\text{cm}^{-1}$  for A) DPPC/DPPCd62 bilayers in the presence of 100 mM KCl (black) and 97 mM KCl + 1 mM  $\text{CaCl}_2$  (blue) recorded at 26.9 and 26.6 °C, respectively; B) 10% DPPS in DPPCd62 bilayers in the presence of 100 mM KCl (black) and 97 mM KCl + 1 mM  $\text{CaCl}_2$  (blue) recorded at 24.7 and 24.5 °C, respectively; C) 10% DPPS in DPPCd62 bilayers in the presence of 100 mM KCl (black) and 97 mM KCl + 1 mM  $\text{MgCl}_2$  (green) recorded at 24.7 and 24.5 °C, respectively. The solid lines in A, B and C are the fits to the data using Equation 7. Figures D and E show the linearized Eyring plots of the measured flip-flop rates for DPPC and 10% DPPS in DPPCd62, respectively obtained in 100 mM KCl (gray circles), 97 mM KCl + 1 mM  $\text{CaCl}_2$  (blue triangles) and 97 mM KCl + 1 mM  $\text{MgCl}_2$  (green squares). The dashed lines are the fits to the data using Equation 21 with the corresponding confidence intervals (solid lines). Figure D also contains measured flip-flop rates for DPPC in the presence of 10% DPPSd62 (red diamonds) with 97 mM KCl + 1 mM  $\text{CaCl}_2$ .



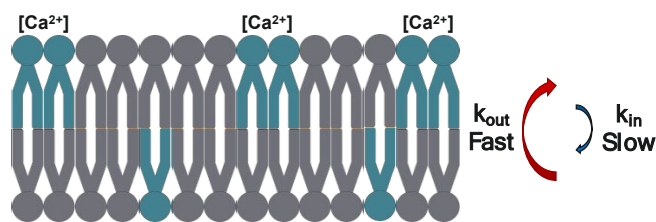


Figure 11: Illustration of the enrichment of PS lipids (blue) on the  $\text{Ca}^{2+}$ -exposed distal leaflet, driven by unequal rates of slow inward flip ( $k_{in}$ ) and fast outward flop ( $k_{out}$ ).

difference in the rate of PS flip and flop (Equation 19).<sup>64, 66, 126</sup> In the case where  $k_{flip} = k_{flop}$ , one would expect the system to mix to homogeneity, where  $N_{proximal} = N_{distal}$ . Such is observed in the flip-flop measurements in Figures 10A-10C, where sum-frequency signal trends toward zero due to the increasing symmetry of the system (Equation 5). However, in the case of unequal rates of  $k_{flip}$  and  $k_{flop}$ , the equilibrium expression (Equation 19) dictates accumulation toward the side of lower  $k$ , as the rate of inward movement is greater than the rate of outward transfer. Using the flip-flop rates determined in Figure 10C as an example, a  $\text{Ca}^{2+}$  concentration whereby the distal leaflet is exposed to 1 mM  $\text{Ca}^{2+}$  while the proximal leaflet is unexposed to  $\text{Ca}^{2+}$  would result in a DPPS  $k_{flip}$  of  $1.46 \pm 0.07 \times 10^{-5} \text{ s}^{-1}$  and  $k_{flop}$  of  $7.11 \pm 0.08 \times 10^{-5} \text{ s}^{-1}$  at 24.5 °C. Applied to Equation 19, DPPS would be expected to enrich in the  $\text{Ca}^{2+}$  exposed leaflet by a factor of 4.87:1, or approximately 80% of the total DPPS population (Figure 11). Ongoing research aims to further validate the Ca-induced PS expression model by way of SFVS of surface-tethered vesicles where the concentration of  $\text{Ca}^{2+}$  of the external and internally encapsulated solution can be independently controlled. From the data shown here, an initially symmetric PS population should produce asymmetric vesicles upon exposure to a calcium concentration gradient and thus yield an increase in sum frequency. Such experiments would additionally allow a comparison of lipid flip-flop rates determined from PSLB and vesicle systems and aid in the examination of inconsistencies between methods.

While the flip-flop rates used in the prior calculation are particular to the non-physiologic binary mixture tested, Ca-PS interactions *in vivo* can reasonably be inferred to slow PS lipid flip-flop in an analogous fashion. The extent of the effect is very likely to depend on the membrane matrix and experimental parameters, which precludes any universal statement on how the effect may manifest. However, the theorized enrichment of PS toward the Ca-exposed leaflet is in agreement with the observations of both the Hampton and Bratton groups where the degree of PS expression was dependent on a  $\text{Ca}^{2+}$  concentration differential over the bilayer as opposed to  $\text{Ca}^{2+}$  influx.<sup>26, 57</sup>

On the surface, migration of PS lipids toward  $\text{Ca}^{2+}$  would seem incompatible with the usual observations of internally held PS, where  $\text{Ca}^{2+}$  content is minimal.<sup>56</sup> However, PS externalization is normally induced *in vivo* by some intentional perturbation of the cells. For example,

common methods of achieving PS externalization include UV irradiation, incorporation of membrane-permeating ionophores, ATP-depletion, deoxygenation, and other treatments which may destabilize cell functioning in some unforeseen ways.<sup>17, 30, 34, 36, 37, 40, 41, 44, 48, 127</sup> As the mechanisms by which PS asymmetry is maintained in healthy cells are not fully understood, the effects of such treatment on the cell's ability to maintain PS asymmetry is not fully detailed. Destabilized cell functionality may simply lead to PS lipids becoming free to equilibrate across the membrane boundary. Many studies on PS externalization utilize high concentrations of external  $\text{Ca}^{2+}$  to mimic physiologic conditions, make use of Ca-dependent Annexin V staining, or test the dependence of scramblases on  $\text{Ca}^{2+}$  content.<sup>2, 4, 12, 18, 20, 25, 26, 29, 32-37, 40, 44, 45, 48, 127-138</sup> Due to PS experiencing differing flip and flop rates, some amount of PS expression may simply be attributed to the high external concentrations of  $\text{Ca}^{2+}$ .

The hypothesized effect of Ca-induced PS enrichment does not preclude the effects of scramblases or signalling processes which may also serve to externalize PS. Multiple pathways of externalization may coexist. The potential presence of a direct PS- $\text{Ca}^{2+}$  mechanism of externalization does however suggest that determinations of cooperative actions between  $\text{Ca}^{2+}$  and scramblases may first require disentanglement from effects driven purely by PS- $\text{Ca}^{2+}$  interactions. The data reported here demonstrates the importance of considering the influence of  $\text{Ca}^{2+}$  concentration differentials when interpreting PS expression data.

## Conclusions

Compression isotherms of DPPC and DPPS monolayers in the presence and absence of 1 mM  $\text{Ca}^{2+}$  or 1 mM  $\text{Mg}^{2+}$  revealed a specific interaction between DPPS and  $\text{Ca}^{2+}$  ions. When in the presence of  $\text{Ca}^{2+}$ , but not  $\text{Mg}^{2+}$ , a  $-2.4 \pm 0.6 \text{ \AA}^2/\text{molecule}$  reduction in the MMA of DPPS was observed at 30 mN/m. No change in MMA was observed for DPPC. A net condensation of the DPPS monolayer in the presence of  $\text{Ca}^{2+}$  is consistent with a headgroup-bridging binding interaction whereby neighboring headgroups are brought into closer contact. A 2:1 PS: $\text{Ca}^{2+}$  binding ratio was hypothesized.

SFVS spectra of DPPS and DPPC hybrid bilayers were examined at concentrations between 0 and 40 mM  $\text{Ca}^{2+}$  or  $\text{Mg}^{2+}$  to determine whether the binding of either  $\text{Ca}^{2+}$  or  $\text{Mg}^{2+}$  to PS or PC headgroups impacted membrane structure. No effect on DPPC was observed for either  $\text{Ca}^{2+}$  or  $\text{Mg}^{2+}$ , whereas DPPS responded to both  $\text{Ca}^{2+}$  and  $\text{Mg}^{2+}$ . As the concentration of  $\text{Ca}^{2+}$  or  $\text{Mg}^{2+}$  was increased, DPPS hybrid bilayers showed an increase in the amine peak sum-frequency at  $3300 \text{ cm}^{-1}$ , as well as decreases in sum-frequency of the ice- and water-like O-H peaks at  $3200 \text{ cm}^{-1}$  and  $3400 \text{ cm}^{-1}$ , respectively. The growth in the amine peak is attributed to complexation of the PS headgroup and ordering of the amine moiety.  $\text{Ca}^{2+}$  ions were shown to





have a more pronounced influence on ordering of the amine groups, resulting in double the  $3300\text{cm}^{-1}$  peak area at saturation when compared to  $\text{Mg}^{2+}$ . Frumkin model binding isotherms were calculated through relation of the change in amine peak area with the bulk concentration of either  $\text{Ca}^{2+}$  or  $\text{Mg}^{2+}$  present. The binding isotherms showed both  $\text{Ca}^{2+}$  and  $\text{Mg}^{2+}$  demonstrate binding behaviors toward PS lipids, with affinity values of  $1.3 \pm 0.3 \times 10^5 \text{ M}^{-1}$  and  $7.3 \pm 2.5 \times 10^3 \text{ M}^{-1}$ , respectively.

The amine peak binding isotherm for  $\text{Ca}^{2+}$  was used in conjunction with the assumed 2:1 PS: $\text{Ca}^{2+}$  binding ratio to calculate the membrane charge state and  $E_{DC}$  field strength. The peak amplitudes of both the ice- and water-like O-H peaks of the DPPS associated water layer were found to track linearly with  $E_{DC}$  values projected from the Ca-PS binding isotherm. These results are in line with  $E_{DC}$  scaling of  $\chi^{(3)}$  and the reorientation of water within the surface charge dependent  $E_{DC}$  field. At saturating concentrations of  $\text{Ca}^{2+}$ , loss of temperature dependence of sum-frequency at the  $3200 \text{ cm}^{-1}$  ice-like water resonance was observed. These data indicate an  $E_{DC}$  of zero and complete charge neutralization at  $\text{Ca}^{2+}$  saturation, consistent with the assumed 2:1 PS: $\text{Ca}^{2+}$  binding ratio.

SFVS measurements of DPPS and DPPC flip-flop rates in the presence and absence of physiologic 1 mM  $\text{Ca}^{2+}$  and 1 mM  $\text{Mg}^{2+}$  were utilized to determine the impact of bound  $\text{Ca}^{2+}$  or  $\text{Mg}^{2+}$  on DPPS and DPPC lipid translocation. The measured rate of translocation of 10% DPPS in DPPC decreased from  $7.11 \pm 0.08 \times 10^{-5} \text{ s}^{-1}$  ( $24.7 \text{ }^\circ\text{C}$ ) in the absence of  $\text{Ca}^{2+}$  to  $1.46 \pm 0.07 \times 10^{-5} \text{ s}^{-1}$  ( $24.5 \text{ }^\circ\text{C}$ ) when in the presence of 1 mM  $\text{Ca}^{2+}$ , roughly a 5-fold decrease. No effect of  $\text{Mg}^{2+}$  on DPPS flip-flop rate or  $\text{Ca}^{2+}$  or  $\text{Mg}^{2+}$  on DPPC flip-flop rate was observed. From these data it is inferred that a  $\text{Ca}^{2+}$  concentration differential over the bilayer would produce differing rates of PS lipid flip and flop between the leaflets. For the tested binary mixture of 10% DPPS in DPPC, the differential in the zero  $\text{Ca}^{2+}$  and 1 mM  $\text{Ca}^{2+}$  flip-flop rates at  $\sim 24.6 \text{ }^\circ\text{C}$  would be expected to result in an approximate 80% sequestration of DPPS toward the  $\text{Ca}^{2+}$ -exposed leaflet. Given the large differential in  $\text{Ca}^{2+}$  concentration over the cell membrane *in vivo*, the endogenous effects of  $\text{Ca}^{2+}$  on PS lipids may influence PS lipid externalization even absent enzymatic action. These results illustrate the importance of considering direct Ca-PS interactions when interpreting PS locality and expression.

## Author contributions

J.C.C and P.P.H designed the research. P.P.H. performed the research. P.P.H. and J.C.C. analysed the data and wrote the article. P.P.H. and J.C.C. edited the manuscript.

## Conflicts of interest

There are no conflicts to declare.

## Data availability

The data that supports these findings are available from the corresponding author upon reasonable request.

## Acknowledgements

The following work was supported by the National Science Foundation (NSF) (No. 2304682).

## Notes and references

‡ Footnotes relating to the main text should appear here. These might include comments relevant not central to the matter under discussion, limited experimental and spectral data, and crystallographic data.

§

§§

etc.

1. R. Chandra, P. C. Joshi, V. K. Bajpai and C. M. Gupta, *Biochim Biophys Acta*, 1987, **902**, 253-262.
2. D. L. Daleke, *Current Opinion in Hematology*, 2008, **15**, 191-195.
3. R. D. Kornberg and H. M. McConnell, *Biochemistry*, 1971, **10**, 1111-1120.
4. G. Lenoir, P. Williamson and J. C. Holthuis, *Current Opinion in Chemical Biology*, 2007, **11**, 654-661.
5. J. A. Op den Kamp, *Annual review of biochemistry*, 1979, **48**, 47-71.
6. A. Martin-Molina, C. Rodriguez-Beas and J. Faraudo, *Biophys J*, 2012, **102**, 2095-2103.
7. A. J. Verkleij, R. F. Zwaal, B. Roelofsen, P. Comfurius, D. Kastelijn and L. L. van Deenen, *Biochim Biophys Acta*, 1973, **323**, 178-193.
8. J. H. Lorent, K. R. Levental, L. Ganesan, G. Rivera-Longworth, E. Sezgin, M. Doktorova, E. Lyman and I. Levental, *Nat Chem Biol*, 2020, **16**, 644-652.
9. G. Cevc, *Biochim Biophys Acta*, 1990, **1031**, 311-382.
10. B. Fadeel and D. Xue, *Critical Reviews in Biochemistry and Molecular Biology*, 2009, **44**, 264-277.
11. N. Duzgunes, J. Wilschut, R. Fraley and D. Papahadjopoulos, *Biochim Biophys Acta*, 1981, **642**, 182-195.
12. J. W. Gauer, K. J. Knutson, S. R. Jaworski, A. M. Rice, A. M. Rannikko, B. R. Lentz and A. Hinderliter, *Biophys J*, 2013, **104**, 2437-2447.
13. J. G. Kay and G. D. Fairn, *Cell Communication and Signaling*, 2019, **17**, 1-8.
14. S. Ohki and R. Sauve, *Biochim Biophys Acta*, 1978, **511**, 377-387.
15. A. Portis, C. Newton, W. Pangborn and D. Papahadjopoulos, *Biochemistry*, 1979, **18**, 780-790.
16. J. Wang, C. Yu, J. Zhuang, W. Qi, J. Jiang, X. Liu, W. Zhao, Y. Cao, H. Wu, J. Qi and R. C. Zhao, *Biomark Res*, 2022, **10**, 4.
17. E. M. Bevers, P. Comfurius and R. F. Zwaal, *Biochim Biophys Acta*, 1983, **736**, 57-66.
18. A. D. Ide, E. M. Wight and C. K. Damer, *PLoS One*, 2021, **16**, e0250710.
19. A. K. Kimura and T. Kimura, *FASEB J*, 2021, **35**, e21177.



20. I. Vermes, C. Haanen, H. Steffens-Nakken and C. Reutelingsperger, *J Immunol Methods*, 1995, **184**, 39-51.
21. P. F. Devaux, A. Herrmann, N. Ohlwein and M. M. Kozlov, *Biochimica et Biophysica Acta - Biomembranes*, 2008, **1778**, 1591-1600.
22. A. Papadopoulos, S. Vehring, I. López-Montero, L. Kutschenko, M. Stöckl, P. F. Devaux, M. Kozlov, T. Pomorski and A. Herrmann, *Journal of Biological Chemistry*, 2007, **282**, 15559-15568.
23. K. Segawa, S. Kurata and S. Nagata, *J Biol Chem*, 2016, **291**, 762-772.
24. K. Segawa, S. Kurata, Y. Yanagihashi, T. R. Brummelkamp, F. Matsuda and S. Nagata, *Science*, 2014, **344**, 1164-1168.
25. H. Takatsu, M. Takayama, T. Naito, N. Takada, K. Tsumagari, Y. Ishihama, K. Nakayama and H. W. Shin, *Nat Commun*, 2017, **8**, 1423.
26. D. L. Bratton, V. A. Fadok, D. A. Richter, J. M. Kailey, L. A. Guthrie and P. M. Henson, *J Biol Chem*, 1997, **272**, 26159-26165.
27. T. Pomorski, A. Herrmann, P. Müller, G. Van Meer and K. Burger, *Biochemistry*, 1999, **38**, 142-150.
28. T. Pomorski, P. Müller, B. Zimmermann, K. Burger, P. F. Devaux and A. Herrmann, *Journal of Cell Science*, 1996, **109**, 687-698.
29. X. Tang, M. S. Halleck, R. A. Schlegel and P. Williamson, *Science*, 1996, **272**, 1495-1497.
30. E. M. Bevers, P. F. Verhallen, A. J. Visser, P. Comfurius and R. F. Zwaal, *Biochemistry*, 1990, **29**, 5132-5137.
31. E. F. Smeets, P. Comfurius, E. M. Bevers and R. F. Zwaal, *Biochim Biophys Acta*, 1994, **1195**, 281-286.
32. E. M. Bevers and P. L. Williamson, *FEBS Lett*, 2010, **584**, 2724-2730.
33. M. Ikeda, A. Kihara and Y. Igarashi, *Biological and Pharmaceutical Bulletin*, 2006, **29**, 1542-1546.
34. A. Momchilova, L. Ivanova, T. Markovska and R. Pankov, *Arch Biochem Biophys*, 2000, **381**, 295-301.
35. J. Suzuki, M. Umeda, P. J. Sims and S. Nagata, *Nature*, 2010, **468**, 834-838.
36. P. Williamson, E. M. Bevers, E. F. Smeets, P. Comfurius, R. A. Schlegel and R. F. Zwaal, *Biochemistry*, 1995, **34**, 10448-10455.
37. P. Williamson, A. Christie, T. Kohlin, R. A. Schlegel, P. Comfurius, M. Harmsma, R. F. Zwaal and E. M. Bevers, *Biochemistry*, 2001, **40**, 8065-8072.
38. M. Seigneuret and P. F. Devaux, *Proceedings of the National Academy of Sciences of the United States of America*, 1984, **81**, 3751-3755.
39. B. J. Abbott, D. S. Fukuda, D. E. Dorman, J. L. Occolowitz, M. Debono and L. Farhner, *Antimicrob Agents Chemother*, 1979, **16**, 808-812.
40. J. Dachary-Prigent, J. M. Pasquet, J. M. Freyssinet and A. T. Nurden, *Biochemistry*, 1995, **34**, 11625-11634.
41. U. Henseleit, G. Plasa and C. Haest, *Biochim Biophys Acta*, 1990, **1029**, 127-135.
42. A. Jaskulska, A. E. Janecka and K. Gach-Janczak, *Int J Mol Sci*, 2020, **22**.
43. J. K. Paterson, K. Renkema, L. Burden, M. S. Halleck, R. A. Schlegel, P. Williamson and D. L. Daleke, *Biochemistry*, 2006, **45**, 5367-5376.
44. P. Williamson, A. Kulick, A. Zachowski, R. A. Schlegel and P. F. Devaux, *Biochemistry*, 1992, **31**, 6355-6360.
45. D. W. Dekkers, P. Comfurius, E. M. Bevers and R. F. Zwaal, *Biochem J*, 2002, **362**, 741-747. DOI: 10.1039/D1FD00206G
46. Q. Zhou, J. Zhao, T. Wiedmer and P. J. Sims, *Blood*, 2002, **99**, 4030-4038.
47. J. R. Nofer, G. Herminghaus, M. Brodde, E. Morgenstern, S. Rust, T. Engel, U. Seedorf, G. Assmann, H. Bluethmann and B. E. Kehrel, *J Biol Chem*, 2004, **279**, 34032-34037.
48. P. Williamson, M. S. Halleck, J. Malowitz, S. Ng, X. Fan, S. Krahling, A. T. Remaley and R. A. Schlegel, *PLoS One*, 2007, **2**, e729.
49. M. Ross, C. Steinem, H.-J. Galla and A. Janshoff, *Langmuir*, 2001, **17**, 2437-2445.
50. K. Jacobson and D. Papahadjopoulos, *Biochemistry*, 1975, **14**, 152-161.
51. D. Papahadjopoulos, G. Poste, B. E. Schaeffer and W. J. Vail, *Biochim Biophys Acta*, 1974, **352**, 10-28.
52. C. Newton, W. Pangborn, S. Nir and D. Papahadjopoulos, *Biochim Biophys Acta*, 1978, **506**, 281-287.
53. D. Papahadjopoulos and A. Portis, *Annals New York Academy of Sciences*, 1978, **05467**, 50-66.
54. D. Papahadjopoulos, W. J. Vail, C. Newton, S. Nir, K. Jacobson, G. Poste and R. Lazo, *Biochim Biophys Acta*, 1977, **465**, 579-598.
55. R. Vink and M. Nechifor, *Magnesium in the Central Nervous System*, University of Adelaide Press, South Australia, 2011.
56. D. K. Atchison and W. H. Beierwaltes, *Pflugers Arch*, 2013, **465**, 59-69.
57. M. B. Hampton, D. M. Vanags, M. I. Porn-Ares and S. Orrenius, *FEBS Lett*, 1996, **399**, 277-282.
58. V. Cheng and J. C. Conboy, *J Phys Chem B*, 2022, **126**, 7651-7663.
59. F. A. Heberle, D. Marquardt, M. Doktorova, B. Geier, R. F. Standaert, P. Heftberger, B. Kollmitzer, J. D. Nickels, R. A. Dick, G. W. Feigenson, J. Katsaras, E. London and G. Pabst, *Langmuir*, 2016, **32**, 5195-5200.
60. M. Nakano, M. Fukuda, T. Kudo, H. Endo and T. Handa, *Physical Review Letters*, 2007, **98**.
61. M. Nakano, M. Fukuda, T. Kudo, N. Matsuzaki, T. Azuma, K. Sekine, H. Endo and T. Handa, *Journal of Physical Chemistry B*, 2009, **113**, 6745-6748.
62. B. Wah, J. M. Breidigan, J. Adams, P. Horbal, S. Garg, L. Porcar and U. Perez-Salas, *Langmuir*, 2017, **33**, 3384-3394.
63. J. S. Allhusen and J. C. Conboy, *Accounts of Chemical Research*, 2017, **50**, 58-65.
64. T. C. Anglin and J. C. Conboy, *Biochemistry*, 2009, **48**, 10220-10234.
65. J. Liu and J. C. Conboy, *Biophysical Journal*, 2005, **89**, 2522-2532.
66. J. Liu and J. C. Conboy, *J Am Chem Soc*, 2004, **126**, 8376-8377.
67. A. Timothy, C. Michael, L. Hao, C. Katherine and C. John, *Journal of Physical Chemistry B*, 2010, **114**, 1903-1914.
68. K. L. Brown and J. C. Conboy, *Journal of Physical Chemistry B*, 2013, **117**, 15041-15050.
69. D. Marquardt, B. Geier and G. Pabst, *Membranes (Basel)*, 2015, **5**, 180-196.
70. D. Marquardt, F. A. Heberle, T. Miti, B. Eicher, E. London, J. Katsaras and G. Pabst, *Langmuir*, 2017, **33**, 3731-3741.



71. M. Doktorova, F. A. Heberle, B. Eicher, R. F. Standaert, J. Katsaras, E. London, G. Pabst and D. Marquardt, *Nat Protoc*, 2018, **13**, 2086-2101.
72. L. Marx, M. P. K. Frewein, E. F. Semeraro, G. N. Rechberger, K. Lohner, L. Porcar and G. Pabst, *Faraday Discuss*, 2021, **232**, 435-447.
73. M. P. K. Frewein, P. Pillar, E. F. Semeraro, K. C. Batchu, F. A. Heberle, H. L. Scott, Y. Gerelli, L. Porcar and G. Pabst, *J Membr Biol*, 2022, **255**, 407-421.
74. H. M. McConnell, L. K. Tamm and R. M. Weis, *Proceedings of the National Academy of Sciences*, 1984, **81**, 3249-3253.
75. M. L. Wagner and L. K. Tamm, *Biophys J*, 2000, **79**, 1400-1414.
76. V. Kiessling and L. K. Tamm, *Biophysical Journal*, 2003, **84**, 408-418.
77. V. Kiessling, C. Wan and L. K. Tamm, *Biochim Biophys Acta*, 2009, **1788**, 64-71.
78. V. Kiessling, J. M. Crane and L. K. Tamm, *Biophys J*, 2006, **91**, 3313-3326.
79. M. Zaccchia, M. L. Abategiovanni, S. Stratigis and G. Capasso, *Kidney Dis (Basel)*, 2016, **2**, 72-79.
80. P. Guyot-Sionnest, J. H. Hunt and Y. R. Shen, *Physical Review Letters*, 1987, **59**, 1597-1600.
81. V. Ostroverkhov, G. A. Waychunas and Y. R. Shen, *Chemical Physics Letters*, 2004, **386**, 144-148.
82. J. Liu and J. C. Conboy, *Langmuir*, 2005, **21**, 9091-9097.
83. D. Marsh, *Biochim Biophys Acta*, 1996, **1286**, 183-223.
84. A. J. Diaz, F. Albertorio, S. Daniel and P. S. Cremer, *Langmuir*, 2008, **24**, 6820-6826.
85. O. Bouffioux, A. Berquand, M. Eeman, M. Paquot, Y. F. Dufrene, R. Brasseur and M. Deleu, *Biochim Biophys Acta*, 2007, **1768**, 1758-1768.
86. J. Miñones, J. M. Rodríguez Patino, O. Conde, C. Carrera and R. Seoane, *Colloids and Surfaces A: Physicochemical and Engineering Aspects*, 2002, **203**, 273-286.
87. E. M. Adams, C. B. Casper and H. C. Allen, *J Colloid Interface Sci*, 2016, **478**, 353-364.
88. S. Narayanan, Doctor of Philosophy, The Pennsylvania State University, 2019.
89. J. T. Davies and E. K. Rideal, *Interfacial Phenomena*, Academic Press, New York, Second edn., 1963.
90. D. Simonelli, S. Baldelli and M. J. Shultz, *Chemical Physics Letters*, 1998, **298**, 400-404.
91. M. L. Clarke, J. Wang and Z. Chen, *J Phys Chem B*, 2005, **109**, 22027-22035.
92. S. Y. Jung, S. M. Lim, F. Albertorio, G. Kim, M. C. Gurau, R. D. Yang, M. A. Holden and P. S. Cremer, *J Am Chem Soc*, 2003, **125**, 12782-12786.
93. T. Weidner, N. F. Breen, G. P. Drobny and D. G. Castner, *J Phys Chem B*, 2009, **113**, 15423-15426.
94. J. Seelig, P. M. Macdonald and P. G. Scherer, *Biochemistry*, 1987, **26**, 7535-7541.
95. T. T. Nguyen and J. C. Conboy, *Anal Chem*, 2011, **83**, 5979-5988.
96. T. T. Nguyen, K. Rembert and J. C. Conboy, *J Am Chem Soc*, 2009, **131**, 1401-1403.
97. H. Hauser, A. Darke and M. C. Phillips, *Eur J Biochem*, 1976, **62**, 335-344.
98. C. G. Sinn, M. Antonietti and R. Dimova, *Colloids and Surfaces A: Physicochemical and Engineering Aspects*, 2006, **282-283**, 410-419.
99. D. E. Gragson and G. L. Richmond, *Journal of the American Chemical Society*, 1998, **120**, 366-375.
100. G. L. Richmond, *Chem Rev*, 2002, **102**, 2693-2724. Online DOI: 10.1029/1045FD00206G
101. A. G. de Beer and S. Roke, *J Chem Phys*, 2016, **145**, 044705.
102. X. Chen, W. Hua, Z. Huang and H. C. Allen, *J Am Chem Soc*, 2010, **132**, 11336-11342.
103. P. E. Ohno, H. F. Wang and F. M. Geiger, *Nat Commun*, 2017, **8**, 1032.
104. P. E. Ohno, H. F. Wang, F. Paesani, J. L. Skinner and F. M. Geiger, *J Phys Chem A*, 2018, **122**, 4457-4464.
105. S. Ong, X. Zhao and K. B. Eisenthal, *Chemical Physics Letters*, 1992, **191**, 327-335.
106. X. Zhao, S. Ong and K. B. Eisenthal, *Chemical Physics Letters*, 1993, **202**, 513-520.
107. B. F. Levine and C. G. Bethea, *The Journal of Chemical Physics*, 1976, **65**, 2429-2438.
108. P. D. Maker and R. W. Terhune, *Physical Review*, 1965, **137**, A801-A818.
109. R. W. Terhune, P. D. Maker and C. M. Savage, *Physical Review Letters*, 1962, **8**, 404-406.
110. S. Kielich, *IEEE Journal of Quantum Electronics*, 1969, **5**, 562-568.
111. G. Gonella, C. Lütgebaucks, A. G. F. de Beer and S. Roke, *The Journal of Physical Chemistry C*, 2016, **120**, 9165-9173.
112. J. A. Armstrong, N. Bloembergen, J. Ducuing and P. S. Pershan, *Physical Review*, 1962, **127**, 1918-1939.
113. P. A. Franken and J. F. Ward, *Reviews of Modern Physics*, 1963, **35**, 23-39.
114. M. A. Habib and J. O. Bockris, *Langmuir*, 2002, **2**, 388-392.
115. A. Chachaj-Brekiesz, J. Kobierski, A. Wnetrzak and P. Dynarowicz-Latka, *Membranes (Basel)*, 2021, **11**.
116. M. Eisenberg, T. Gresalfi, T. Riccio and S. McLaughlin, *Biochemistry*, 1979, **18**, 5213-5223.
117. Y. A. Ermakov, *Membranes (Basel)*, 2023, **13**.
118. P. Debye and E. Hückel, *Physikalische Zeitschrift*, 1923, **24**, 185-206.
119. J. C. Conboy, M. C. Messmer and G. L. Richmond, *Langmuir*, 1998, **14**, 6722-6727.
120. J. C. Conboy, M. C. Messmer and G. L. Richmond, *The Journal of Physical Chemistry*, 1996, **100**, 7617-7622.
121. R. N. Ward, D. C. Duffy, P. B. Davies and C. D. Bain, *The Journal of Physical Chemistry*, 2002, **98**, 8536-8542.
122. X. Zhuang, P. B. Miranda, D. Kim and Y. R. Shen, *Physical Review B*, 1999, **59**, 12632-12640.
123. R. Mendelsohn, M. A. Davies, J. W. Brauner, H. F. Schuster and R. A. Dluhy, *Biochemistry*, 1989, **28**, 8934-8939.
124. J. r. Tuchtenhagen, W. Ziegler and A. Blume, *European Biophysics Journal*, 1994, **23**.
125. H. Eyring, *The Journal of Chemical Physics*, 1935, **3**, 107-115.
126. C. M. Guldberg and P. Waage, *Forhandlinger i Videnskabs-Selskabet i Christiania*, 1864, 35-45.
127. E. Weiss, D. C. Rees and J. S. Gibson, *Anemia*, 2011, **2011**, 379894.
128. P. Meers, D. Daleke, K. Hong and D. Papahadjopoulos, *Biochemistry*, 1991, **30**, 2903-2908.
129. P. Raynal and H. B. Pollard, *Biochim Biophys Acta*, 1994, **1197**, 63-93.



## Journal Name

## ARTICLE

130. M. A. Swairjo, N. O. Concha, M. A. Kaetzel, J. R. Dedman and B. A. Seaton, *Nat Struct Biol*, 1995, **2**, 968-974.
131. G. Kohler, U. Hering, O. Zschornig and K. Arnold, *Biochemistry*, 1997, **36**, 8189-8194.
132. K. Balasubramanian, E. M. Bevers, G. M. Willems and A. J. Schroit, *Biochemistry*, 2001, **40**, 8672-8676.
133. K. G. Maffey, L. B. Keil and V. A. DeBari, *Ann Clin Lab Sci*, 2001, **31**, 85-90.
134. J. F. Tait, D. F. Gibson and C. Smith, *Anal Biochem*, 2004, **329**, 112-119.
135. M. A. Lizarbe, J. I. Barrasa, N. Olmo, F. Gavilanes and J. Turnay, *Int J Mol Sci*, 2013, **14**, 2652-2683.
136. H. Yang, A. Kim, T. David, D. Palmer, T. Jin, J. Tien, F. Huang, T. Cheng, S. R. Coughlin, Y. N. Jan and L. Y. Jan, *Cell*, 2012, **151**, 111-122.
137. Y. Furuta, O. Pena-Ramos, Z. Li, L. Chiao and Z. Zhou, *PLoS Genet*, 2021, **17**, e1009066.
138. T. Sakuragi and S. Nagata, *Nat Rev Mol Cell Biol*, 2023, **24**, 576-596.

View Article Online  
DOI: 10.1039/D4FD00206G

Open Access Article. Published on 18 February 2025. Downloaded on 2/21/2025 10:36:05 AM.  
This article is licensed under a Creative Commons Attribution-NonCommercial 3.0 Unported Licence.



Faraday Discussions Accepted Manuscript

**Data Availability Statement:**

The data that support the findings of this study are available from the corresponding author, upon request.

